Thesis for The Degree of Licentiate of Engineering

High Temperature Corrosion in Alkali Fluoride Salts Containing Oxygen

Aida Nikbakht

Department of Chemistry and Chemical Engineering

CHALMERS UNIVERSITY OF TECHNOLOGY

Gothenburg, Sweden 2025

Abstract

Alkali fluoride salts, particularly sodium fluoride (NaF) and lithium fluoride (LiF), play a crucial role in diverse industrial processes, including nuclear reactors, thermal energy storage, battery production and recycling. In their molten state, these salts are valued for their low vapor pressure, high thermal stability, and excellent fluxing properties. However, high-temperature corrosion of containment materials remains a significant challenge in both oxygen-rich and oxygen-depleted environments. Such corrosion can lead to equipment failure, plant shutdowns, premature decommissioning, and considerable financial losses.

This thesis investigates the mechanisms of high-temperature corrosion in contact with alkali fluoride salts, with a focus on NaF and LiF. The primary objective is to elucidate the corrosion behavior of alloying elements, particularly within Inconel 625. Thermodynamic calculations were employed to predict the stability and dissolution tendencies of various alloying elements, and these predictions were validated through experimental analyses.

Fluoride salts degrade protective oxide layers on metals, promoting the formation of transition metal fluorides and subsequent dissolution of alloy components. A detailed comparison between NaF and LiF exposures revealed a distinct influence of the salt type on the corrosion mechanism. No transition metal fluorides were formed during NaF exposure, while LiF exposure resulted in the formation of FeF_2, CrF_2, CrF_3, and NbF_5. Notably, NaF caused significant oxide spallation, indicating a more aggressive attack on the alloy surface.

Temperature gradients, commonly encountered in industries utilizing molten salts, were also examined as a driving factor for corrosion. A comparative study between isothermal and thermal-gradient exposures demonstrated that thermal gradients exacerbate intergranular attack due to galvanic effects, highlighting the importance of temperature control in mitigating corrosion.

Overall, this work provides new insights into the corrosion mechanisms of Inconel 625 in alkali fluoride salts, with emphasis on the role of salt composition and thermal conditions. These findings contribute to the development of more corrosion-resistant materials and optimized operational strategies for high-temperature salt-based applications.

Keywords: Alkali Fluoride Corrosion, Temperature Gradient, Lithium Detection, Metal Fluorides, Redox, High Temperature Corrosion

Acknowledgements

In a month from now it will be three years since I was offered this position. From that day to the moment, there have been people who have supported me in different aspects. I would like to seize this opportunity and express my gratitude to them.

First and foremost, I am immensely thankful to my main supervisor Associate Prof, Christine Geers for trusting me and giving me this opportunity. Your eagerness to discuss with me is invaluable. The constructive comments I get from you and our discussions teaches me a train of thought which helps me formulate my research, this is priceless to me. I also owe my profound gratitude to Dr. Behnam Bahramian, my co-supervisor who has provided me with insightful comments, industrial expertise and interesting research questions.

I am truly thankful to Umicore for their financial support and more importantly their interest in hearing about my results. Thank you for providing me with the opportunity to visit the site in person and discuss with the experts in different sections. I would also like to thank Dr. Hachi Yagi for our engaging discussions and fruitful talks.

Furthermore, I would also like to thank the director of my studies Prof. Itai Panas. Thank you for your continuous support from the moment I entered Sweden till today when we had an amazing scientific discussion. I would also like to thank my examiner, Prof. Martin Andersson for his support and interest in my work.

My heartfelt gratefulness goes to Marredy Reddy, Esraa Hamdy, Vicent Ssenteza, and Loli who were all up for teaching me on the instruments in the beginning and made me feel welcome and home here. I would also like to thank my current colleagues Ageo Meier, Pavan Aletti and Hampus Lindmark for valuable inputs and intriguing discussions.

Special thanks to Hooman Karimi, Thorbjørn Krogsgaard, Shrikanth Syamprasad and Athira Anil who make our department a better place to work at. I would also like to thank my former student Robin Guynot, who assisted me in carrying out the experimental work.

Special thanks to Sandra, our administrator, who has helped me in all the administrative work since the day I got the position.

Finally, I would like to thank those whom talking to gives me energy to work here, my dad with his heartfelt messages every morning, my mom for her belief in me and my decisions, thank you for your unconditional love and all-out support. Special thanks to Ebi, my uncle, who I owe a lot, Nasim and Nastaran for making the distances look invisible with our heartfelt talks. Lastly but most importantly, I would like to thank my partner, Oscar. Your love, support and patience made a turning point in my life and your discipline taught me a lot. I was lucky to have you besides me throughout these years, difficult days have been way easier to go through with you.

Aida Nikbakht,
August 2025

List of Publications

Paper I: published

Nikbakht, A., B. Bahramian, and C. Geers, ***"Deep Intergranular Fluoride Attack by High-Temperature Corrosion on Alloy 625 by LiF in Air at 600° C".*** High Temperature Corrosion of Materials, 2024. **101**(5): p. 1055-1066.

Paper П: under review

Nikbakht, A., B. Bahramian, P. Malmberg and C. Geers ***"Redox Mechanisms and Metal Fluoride Stability in Alkali Fluoride Corrosion-Confirmed by Experiment".*** Available at SSRN 5271372.

Statement of author's contribution:

Paper I: The original draft has been written by me. I performed most of the experiments and the post analysis in both works. Comments from the co-authors have been applied by me into the work.

Paper П: The original draft of both papers have been written by me. I performed most of the experiments and the post analysis in both works. Part of the post exposure analysis in this work (SIMS analysis) was carried out by Per Malmberg and Elias Ranjbari.

List of Acronyms

LIBs	Lithium-ion Batteries
SEM	Scanning Electron Microscopy
SE	Secondary Electrons (in SEM)
BSE	Backscattered Electrons (in SEM)
EDS	Energy Dispersive X-ray Spectroscopy
SIMS	Secondary Ion Mass Spectroscopy
TOF-SIMS	Time of Flight Secondary Ion Mass Spectroscopy
XRD	X-ray Diffraction
LMIG	Liquid Metal Ion Gun
EU	European Union
kWh	Kilowatt-hour
NMC	Nickel–Manganese–Cobalt (battery chemistry)
HF	Hydrogen Fluoride

Contents

1. Introduction

The use of lithium-ion batteries (LIBs) has grown rapidly in recent years, primarily because they serve as key electrical power sources in a wide range of modern electronic devices such as mobile phones, personal computers, and video cameras. LIBs not only lead the market in powering cell phones and laptops, but they are also expected to become the primary choice for powering electric vehicles in the near future [1].

As can be seen in figure 1, between 2012 and 2022, the EU saw a 41% increase in the production of portable batteries, rising from 173,000 to 244,000 tons. Over the same period, the collection of end-of-life batteries for recycling grew even more significantly, by 68%, from 66,000 tons in 2012 to 111,000 tons in 2022 [2]. Despite the surge in battery production, the increase in the volume of unrecycled batteries has been relatively modest. In 2012, approximately 107,000 tons of batteries were not recycled, while by 2022, this figure had grown to 133,000 tons, a rise of just 24% over a decade.

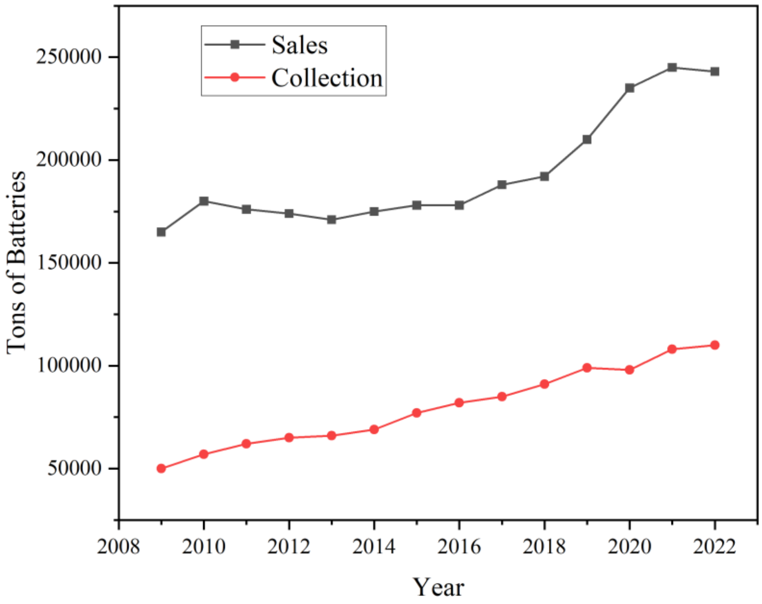

Figure 1) The trends for sales and collection of portable batteries in the EU from 2009 to 2022.

Battery manufacturing is intrinsically associated with greenhouse-gas emissions, commonly reported as carbon-dioxide equivalents (CO_2-eq). For the dominant nickel–manganese–cobalt (NMC) chemistry, the Swedish Energy Agency estimates a specific emission factor of 61–

106kg CO_2-eq $kWh^{-1}$of installed capacity [3]. Using annual production data for Europe from 2010 to 2022, the corresponding cumulative emissions were calculated and are illustrated in figure 2. The line graph for the new production shows a significant increase in the amount of released CO_2 in the atmosphere during the last few years. The newly produced batteries in 2022 have led to a 43% increase in CO_2 emissions in comparison with 2012. Battery recycling as well causes an inevitable amount of CO_2 emission. Based on the results from the Swedish Energy Agency, battery recycling causes 15kg of CO_2 per equivalent kWh battery. The amount of batteries recycled in Europe which were presented in figure 1, were then multiplied by the amount of CO_2 emission in recycling and the data is plotted in the red line in figure 2. As can be seen in figure 2, the amount of CO_2 emissions from new battery production has not been hampered by the recycling strategies and shows a significant increase in CO_2 emissions.

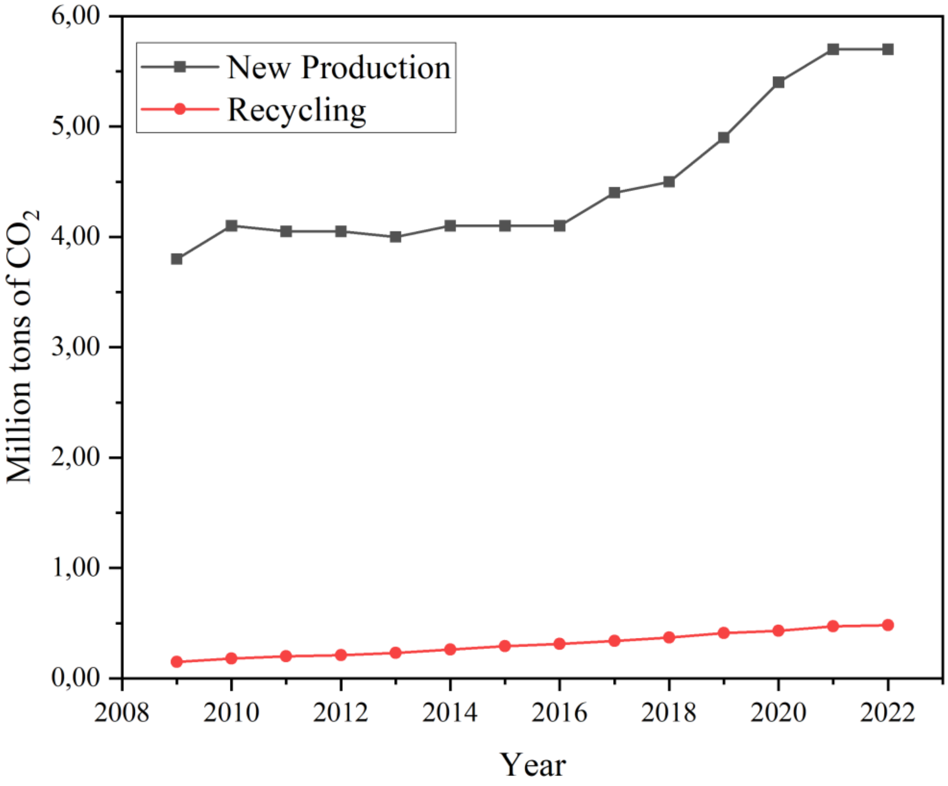

Figure 2) Annual greenhouse gas emissions associated with battery production and recycling from 2009 to 2022.

Beyond concerns related to greenhouse gas emissions, the increasing production of batteries has raised alarms about a potential shortage of critical natural resources such as lithium, cobalt, nickel, and manganese in the coming years. Lithium-ion batteries (LIBs) contain valuable metals (Ni, Li, Co, Cu, Mn, Fe, and Al) as well as toxic substances that pose significant environmental and health hazards [4]. The combined issues of CO_2 emissions from battery manufacturing, limited availability of raw materials, and the presence of hazardous components in LIBs underscore the urgent need for effective recycling strategies.

Currently, spent lithium-ion batteries are recycled via three main pathways: pyrometallurgical smelting, hydrometallurgical leaching, and direct recycling [5]. Hydrometallurgical processing begins with a preparatory phase in which batteries are first discharged, then dismantled, sorted, and mechanically reduced (crushing and shredding) to produce a black mass of cathode and anode materials. The resultant black mass undergoes leaching followed by solvent extraction, ion-exchange, and other downstream operations to isolate and recover critical metals (Li, Mn, Ni, Al, Co) [6, 7].

In pyrometallurgy, spent LIBs are heated in a furnace at elevated temperatures to convert metal oxides into an alloy, generally through sequential smelting and roasting/calcination operations. During heating, all organic and volatile battery components (electrolyte, separator, binder) are combusted, and while very high temperatures promote chemical reduction pathways, comparatively lower temperatures induce phase-change phenomena [7].

The pyrometallurgical recycling of lithium-ion batteries yields three primary output streams: molten metal alloys, mineral slags, and process off-gases. Both the cathode material and the electrolyte contain lithium, and the electrolyte also carries fluorine, hence, corrosive lithium and fluorine bearing species appear in these by-products. These species can get into contact with the metallic material designed to purify the recycled alloy or to purify the toxic gases which are produced. Before release, the hot off gas (≈ 1400 °C as it exits the smelter) enters a metal post-combustion chamber where the recycled alloy is refined and toxic volatiles are treated. Downstream, environmental standards require the flue dust to leave the gas-cleaning section at temperatures below 100 °C. Hence a temperature gradient will occur in the metal material designed to work as the post-combustion chamber.

Having lithium and fluoride species in the metallic system of post- combustion chamber causes corrosion in high temperatures in an oxidizing condition. Corrosion in alkali halogenides and specifically alkali fluorides have been extensively investigated in literature [8-13]. Most of these studies concentrate on non-oxidizing environments (where they can have impurity oxygen and/or humidity) since they mostly have nuclear applications. In the current study however, the environment is oxidizing since post-combustion takes place in air. Although the extent of corrosion attack in the current study is higher, still the fundamentals are comparable.

Inconel 625 is chosen as the main alloy to be tested in high temperature corrosion conditions in two different alkali fluoride salts: lithium fluoride (LiF) and sodium fluoride (NaF). The aim of the thesis is to elucidate how salt chemistry and temperature gradients influence the corrosion process. The thesis is a combination of two papers, the first paper deals with three different scenarios of isothermal and temperature gradient exposures. These scenarios helped to compare the effect the amount of salt can have and clarified the effect of the sample being part of a temperature gradient exposure.

The second paper compares alloy degradation in contact with LiF to that observed with NaF, supported by thermodynamic calculations in each case, which reveal a significant disparity in metal fluoride formation. Literature surveys indicate that fluorine gas is often included in thermodynamic models of metal fluorides, thereby decoupling metal fluoride formation from the specific alkali fluoride salt and the oxidizing species involved. Corrosion mechanisms are proposed for both LiF and NaF exposures, aligning with the corresponding thermodynamic predictions. Given that the inclusion of fluorine gas in previous calculations has been associated with the “active oxidation” corrosion mechanism, thermodynamic analyses were conducted accordingly, ultimately ruling out active oxidation due to the high stability of the alkali fluorides.

2.Background

2.1 Lithium-ion Battery Components and Materials

Irrespective of the cell's external geometry, a lithium-ion battery comprises five principal constituents: a cathode (≈ 22–25 wt %), a separator (≈ 4–5 wt %), an anode (≈ 24–26 wt %), an electrolyte (≈ 10–12 wt %), and a casing or housing (≈ 4–6 wt %) [14].

Cathode: The cathode plays a central role in the battery's function and is typically coated onto aluminum foil, which improves both its efficiency and lifespan. Cathode materials include carbon powder, PVDF binder, and various lithium-based transition metal oxides LiM_xO_y [4].

Anode: Graphite remains the leading anode material in commercial Li-ion batteries due to its low cost, structural stability, and favorable electrochemical properties. It accommodates lithium through intercalation between graphene layers and offers reliable cycling performance [15].

Electrolyte: Ion transport between the anode and cathode during charging and discharging is facilitated by the electrolyte. The most prevalent form is the non-aqueous liquid electrolyte, typically a multicomponent formulation containing a lithium salt dissolved in a blend of organic solvents and various additives. $LiPF_6$ remains the preferred choice not for its exceptional characteristics, but due to the absence of significant drawbacks. Nonetheless, alternative lithium salts, including borates ($LiBF_4$, LiBOB, LiDFOB), and lithium perchlorate ($LiClO_4$), are under consideration as potential replacements [16, 17].

Separator: Among the critical components, battery separator plays a central role in ensuring the overall safety of lithium-ion batteries. Its primary function is to physically separate the anode and cathode while permitting the bidirectional transport of mobile lithium ions, hence it affects the electrochemical stability and performance in lithium-ion batteries. Battery separators are typically manufactured using polyolefins such as polypropylene (PP) and polyethylene (PE), which serve as standard material choices [18].

2.2 Drivers for Recycling Lithium-ion Batteries

Spent lithium-ion batteries (LiBs) typically contain 5%–20% cobalt (Co), 5%–10% nickel (Ni), 5%–7% lithium (Li), and 5%–10% of other metals such as copper (Cu), aluminum (Al), and iron (Fe), along with approximately 15% organic compounds and 7% plastics [10]. However, the exact composition varies by manufacturer. The recovery of valuable metals such as lithium, nickel, cobalt, and manganese (Mn) from spent LiBs offers substantial economic advantages [19].

In addition, LiBs are classified as hazardous waste due to the presence of various toxic elements, and their improper disposal can cause severe environmental harm, including groundwater and soil contamination [6, 20]. Nevertheless, the primary driver for lithium-ion battery (LiB) recycling is the reliance on raw materials used in LiB technology, notably lithium, cobalt, and natural graphite, all of which are listed as Critical Raw Materials (CRMs) in the 2020 classification [5].

Currently, two main principal recycling pathways are employed to convert spent lithium-ion batteries (LiBs) into usable products, classified according to the mechanism by which elements are extracted from electrode active materials: smelting in pyrometallurgy and leaching in hydrometallurgy [5]. The pyrometallurgical method is more of interest in this study, hence the process is summarized below.

2.3 Pyrometallurgical Recycling of LIBs

Disassembled battery cells are blended with limestone ($CaCO_3$), sand, coke, and reducing agents such as metallic aluminum (Al) and zinc (Zn). To ensure economically viable cobalt (Co) and nickel (Ni) yields, the feedstock must consist of 30–50 wt% spent batteries. This mixture is introduced into a vertical shaft furnace equipped with a top submerged lance which is shown in figure 3 [21]. In the initial "preheating zone" (≤300 °C), the electrolyte evaporates slowly, mitigating the risk of explosion [22].

In the subsequent "plastics pyrolysis zone," the temperature rises to approximately 700 °C, causing the plastic components and binders to melt, decompose, and partially evaporate. This is an exothermic process in which the combustion of organic species contributes to heating the upward-flowing gases. These gases, now carrying electrolyte vapors, ascend into the preheating zone and are then directed to the flue gas treatment unit starting from the exhaust chamber.

In the third stage of the vertical shaft furnace, the "smelting and reduction zone," pre-heated air at 500 °C is injected into the furnace base. Within this zone, operating at 1200–1450 °C, residual battery materials are converted into two primary products: a slag phase containing Li, Al, Si, Mn, Ca, and Fe; and a metallic alloy mainly comprising Cu, Co, Ni, and reduced Fe [5, 23].

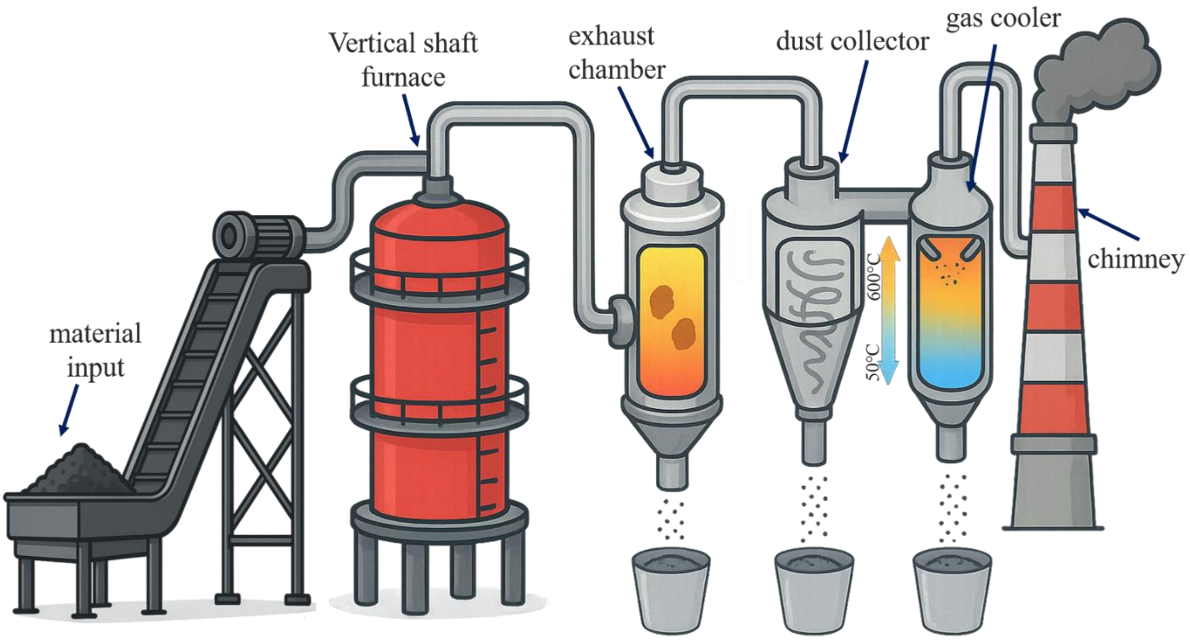

Figure 3) schematic representation of the pyrometallurgical and post-combustion process used in battery recycling, inspired by [24].

Before entering the post-combustion chamber, the temperature of the flue gas emitted from the furnace is raised to 1150 °C using a plasma torch. The hot gases are subsequently quenched to 300 °C using water vapor, followed by conventional filtration. [25, 26]. As shown in figure 3, the exhaust gases enter a cyclone dust collector where the fine powder particles are collected. After the residual exhaust gas is burnt, the remnants in the flue gas are passed through a gas cooler and a bag filter to make them harmless [24].

The high temperature gas cleaning system, powered by the plasma torch, ensures complete decomposition of organic compounds and prevents the formation of harmful dioxins. Halogen-containing compounds are retained in the flue dust, which is subsequently filtered and disposed of [25, 26].

2.4 Corrosion in Salt Environments

Salts, composed of ionic species, become electrically conductive fluids upon melting. They exhibit strong solvating capabilities for metal salts and are capable of sustaining electrochemical corrosion processes. The governing principles of electrochemistry and the associated corrosion mechanisms in molten salts are, to a large extent, comparable to those in aqueous solutions. In this study, salts are categorized into two groups: oxyanion-containing salts and alkali halides, with specific emphasis on alkali fluorides. The following section briefly examines corrosion phenomena in each category, while the remainder of the study focuses on corrosion in alkali fluoride salts, with a detailed investigation of their corrosion causes and mechanisms.

2.4.1 Corrosion in oxyanion-containing salts

These are salts which contain sulfates (SO_4^{2-}), nitrates (NO_3^-), phosphates (PO_4^{3-}), hydroxide (OH^-) and carbonates (CO_3^{2-}). These salts inherently contain oxygen ions as part of their molecular structure. In this case the salt components (SO_4^{2-}, NO_3^-, PO_4^{3-}, OH^- and CO_3^{2-}) can act as metal oxidizers. Their oxidizing characteristics and the products of their reduction vary depending on the chemical activity of the metal being in contact with them. In the following reactions in molten baths of oxygen containing salts, zirconium has been taken as an example for a metal with a higher redox activity and iron as one with a lower redox activity. As can be seen in reaction 1, the more redox active zirconium reduces carbonate ions to elemental carbon, while in reaction 2, iron reduces them only to carbon monoxide. The oxygen ions released from these anions can combine with the metal ions to form oxides [27].

$$Zr_{(s)} + M_2CO_{3(melt)} = ZrO_{2\,(s)} + C_s + M_2O_{(melt)} \qquad R\ 1$$

$$Fe_{(s)} + M_2CO_{3(melt)} = FeO_{\,(s)} + CO_{gas} + M_2O_{(melt)} \qquad R\ 2$$

2.4.2 Fundamentals of Corrosion in alkali halides (non-oxyanion salts)

Simple halide salts that do not contain oxygen in their anions, including fluorides and chlorides like LiF, NaF, LiCl, and NaCl. In a “completely purified” alkali halide salt where there is no oxygen or humidity, pure molten fluoride salts will not react to the alloys in contact to them. This is due to the high stability (negative free energy) of alkali fluoride salts which makes them weak oxidizers of metals [12, 28]. In other words, in the absence of an oxidizing environment (ranging from air to oxygen or water impurities) the salt needs to oxidize the metal. This would mean that the salt cations need to reduce to the elemental state or a lower valency state, which makes alkali metals the weakest oxidizers of metal [27]. Hence, pure fluoride salts will not react with alloys in contact with them. This would mean that the corrosion of alloys in contact with alkali fluoride salts is derived by oxygen in oxidizing environments or by impurities of water, HF, metal oxides and dissolved polyvalent foreign cations (metal cations) that can oxidize other less noble metals [12].

Considering the fact that almost always there is an inevitable amount of impurity in the system, corrosion with alkali halides in general and alkali fluorides in particular takes place. In the following, we study corrosion in halide salts, with an analogy between molten salt environment and aqueous solutions.

Here we move into indirect acidity, influenced by impurities of moisture and oxygen. Understanding the rate-controlling step in the corrosion mechanism for salts in the second category (alkali halides) was the central goal of a study by Mansfeld et al. [29].

To consider the effect of oxygen, first we start with O_2/O^{2-} equilibrium:

$$\frac{1}{2}O_2 + 2e^- \rightleftharpoons O^{2-} \qquad R\ 3$$

According to the Lux-Flood acid-base theory, acids are defined as oxide ion (O^{2-}) acceptors, while bases are oxide ion donors. This framework allows for the introduction of a concept analogous to pH in aqueous systems, but applicable to oxide-based molten salts [29]:

$$pO^{2-} = -log a_{O^{2-}} \qquad R\ 4$$

This leads to a Nernst-type equation for the reversible potential of the melt:

$$\emptyset_{rev} = \emptyset_{rev}^0 + \frac{2.3RT}{2F} log \frac{\sqrt{p_{O_2}}}{a_{O^{2-}}} \qquad R\ 5$$

By replacing:

$$pO^{2-} = -log a_{O^{2-}} \qquad R\ 6$$

If we consider Q_{rev} to represent the reversible potential of the melt:

$$\emptyset_{rev} = \emptyset_{rev}^0 + \frac{2.3RT}{4F} log p_{O_2} + \frac{2.3RT}{2F}\ pO^{2-} \qquad R\ 7$$

This formulation shows that both an increase in oxygen partial pressure (p_{O_2}) and an increase in oxide ion activity (i.e., a more acidic melt) shift the redox potential of the melt in the noble (positive) direction [27]. Such a shift in potential means that the melt becomes more oxidizing (more electrochemically aggressive) which leads to higher corrosion rates, as reflected by increased corrosion current densities (e.g., in A/cm²). This correlation has been illustrated in figure 4 where higher partial pressures of oxygen have led to higher redox potential in the melt and higher corrosion current.

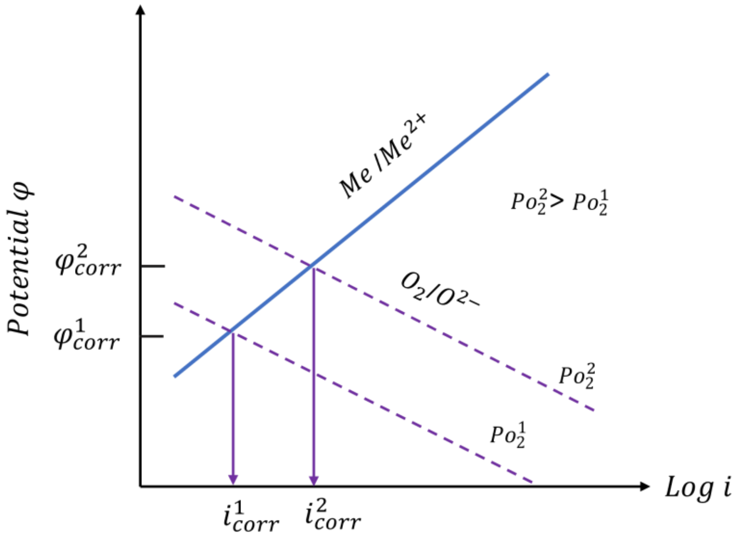

Figure 4)The effect of oxygen partial pressure on corrosion rates in molten salts, adapted from [29].

2.5 Mechanisms and Drivers of Corrosion in Alkali Fluoride Systems

In the complete absence of water and oxygen impurities, molten alkali fluoride salts do not possess a sufficient thermodynamic driving force to induce corrosion of metals; consequently, under these conditions, the salts remain chemically inert with respect to alloy constituents [12, 27, 29].

In experiments which are attempted to minimize the oxidizing components, salts usually go through a purification process with H_2 or HF gas [30]. For processes which are attempted to be conducted in non-oxidizing atmospheres, it is essential to purify fluoride salts to eliminate oxide impurities and residual moisture. This is commonly achieved by sparging the molten salt with an HF/H_2 gas mixture, which serves a dual purpose. The HF reacts with metal oxides, converting them into their corresponding fluorides and releasing water vapor [12], as illustrated in the following reactions:

$$2HF(g) + A_2O(dissolved) \leftrightarrow 2AF(d) + H_2O(g) \qquad A = Alkali\ metal$$ *R 8*

Simultaneously, the presence of H_2 suppresses corrosion of the alloy by HF, enabling a controlled purification process. This treatment effectively reduces the oxide content and residual water, thereby ensuring the molten salt's compatibility with sensitive, oxygen-free operational environments.

However, a study aimed at purifying FLiBe by injecting HF and H_2, revealed that approximately 180 ppm of trace HF remained dissolved in the salt [30]. Kondo et al. reported a constant HF concentration, implying that HF formation occurred during salt exposure. In parallel, Olson et al. recognized the potential impact of trace impurities on corrosion processes, despite this aspect not being central to their study [8].

In the following section, the common impurities which are considered as drivers of corrosion in alkali fluorides in an attempted non-oxidizing environment will be discussed in more detail.

2.5.1 Common Corrosive Agents in Molten Fluoride Salts

In order to examine corrosion in alkali fluoride salts, it is important to recognize what the oxidizing agents in the salt are. In this section we will talk about different oxidizing agents like HF, water or oxygen which are possible to exist in the system.

a) HF can react with active metals such as Cr, causing corrosion. The presence of moisture in fluoride salts can lead to the formation of hydrofluoric acid which is highly corrosive [28]. As shown in reaction 12, residual water can hydrolyze the salts at high temperatures, leading to the formation of HF and the corresponding oxide. The produced HF can then react with different alloying elements from the metal, forming metal fluorides as shown in reaction 13. By the oxidation of the metal, leading to the formation of metal fluorides, hydrogen can get reduced at the same time [12].

$$2AF + H_2O = A_2O + 2HF \qquad (A = Li, Na, K) \qquad \textit{R 9}$$

$$M + yHF = MF_y + \frac{y}{2}H_2 \qquad \textit{R 10}$$

a) High valency cations of polyvalent transition metals such as Fe^{3+} and Cr^{3+} are able to oxidize their own base metals and cause corrosion [12].

$$2Cr^{3+} + Cr^0 \leftrightarrow 3Cr^{2+} \qquad \textit{R 11}$$

b) Metallic impurities in the salt such as Fe which are incorporated as metal fluorides in the process of manufacturing the salt can react with less noble alloying elements such as Cr and result in corrosion reactions [28, 31]:

$FeF_2 + Cr = CrF_2 + Fe$ R 12

2.5.2 Galvanic Corrosion

When two metals possessing distinct electromotive potentials are electrically connected in the presence of an electrolyte, galvanic corrosion may occur. In this system, the electrolyte completes the electrical circuit by enabling electron and ion flow; the potential difference causes the anodic metal to oxidize, with metal ions transported via the electrolyte (such as molten salt) and ultimately reduced and deposited onto the cathodic metal, provided the metals could form alloys with each other [12, 32].

The galvanic process is intensified when deposition is promoted through the formation of an insoluble alloy or compound (e.g., a carbide) with the cathodic substrate. This process is also influenced by physical parameters, such as the ratio of anode to cathode surface area; specifically, a smaller anodic surface relative to the cathode leads to significantly more aggressive corrosion [32].

Oxidation at the anode: $Cr^0 \leftrightarrow Cr^{2+} + 2e^-$ R 13

Disproportionation at the cathode: $3Cr^{2+} \leftrightarrow 2Cr^{3+} + Cr^0(M)_{alloy}$ R 14

Oxidation and reduction at the anode: $2Cr^{3+} + Cr^0 \leftrightarrow 3Cr^{2+}$ R 15

As can be seen in the reactions above, as long as reaction 13 is initiated, and metal anion is produced, precipitation on the cathode and dissolution on the anode can continue in a cyclic manner. The disproportionation product which is Cr^{3+} can accelerate the corrosion in this case by dissolving more Cr at the anodic site [27]. The rate of this type of corrosion increases with rising temperature, enhanced fluxing of the molten bath, and a larger surface area of the electromotive metal [27].

A similar process was also observed in the study by Olson where the graphite crucibles were of a more cathodic potential in comparison with the Incoloy 800H in FLiNaK salt. This led to a corrosion rate 30 times higher than that in Incoloy 800H crucible [8]. In a case study by Kondo, corrosion tests on ferritic steel, JLF-1 (8.92Cr-2W) revealed that utilizing a nickel crucible resulted in a corrosion rate approximately three times higher than that observed with a JLF-1 crucible. Notably, in another sample where a Nb crucible was used, Nb dissolved from the crucible and redeposited onto the specimen surface. Here, Nb functioned as a sacrificial anode, effectively protecting the sample's constituent elements from dissolution [30].

Both macroscopic and microscopic forms of galvanic corrosion are possible. Although the galvanic effect is typically attributed to dissimilar metals in contact with an electrolyte like molten salt at the component level, it can also occur within nominally homogeneous materials [11]. Studies on molybdenum carbides in different microstructures have shown that they tend to act as cathode in the microstructure [33]. The alloy surface consisting of different elements including Cr is less noble than the Mo rich carbides, hence a micro-galvanic cell forms. The Mo rich particles acting as cathode and the surface around the carbides act as anode, accelerating the corrosion rate [33]. Similar reasoning has been discussed in case of intermetallic phases and the alloy matrix [8].

2.5.3 Temperature Gradient Effects

In a static, isothermal molten salt system, the corrosion of soluble fluorides and chlorides may be constrained by the saturation solubility of transition metal ions. However, in systems exhibiting significant temperature gradients, differential solubility of corrosion products can drive persistent, long-term corrosion processes. The saturation solubility of transition metal halides is strongly temperature-dependent; thus, a thermal gradient within the molten salt establishes a corresponding solubility gradient of dissolved metal ions, which in turn generates an electrochemical potential gradient. This gradient facilitates the oxidation and dissolution of anodic alloy constituents in the hot, unsaturated region of the system, followed by their subsequent re-deposition in the cold, saturated region. If the temperature gradient is sufficient to initiate convective flow within the molten salt and maintain undersaturation in the hot leg, the resulting dissolution–deposition cycle can perpetuate a sustained corrosion mechanism [9, 12].

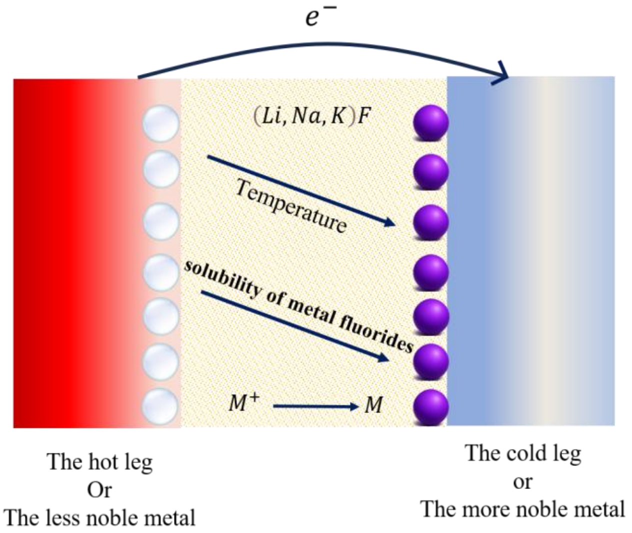

Figure 5) schematic diagram for corrosion in the presence of temperature gradient adapted from [9].

As can be seen in figure 5, a negative gradient for the equilibrium concentration of metal fluorides exists on the surface of the alloy/melt from the hot leg to the cold leg of the samples. Reactions 13-15 are also valid in thermal gradient driven corrosion as well. In this process anodic species can adopt multiple valence states within the molten salt. In such cases, multivalent transition metal cations may undergo disproportionation at the cathodic and interface, yielding both higher-valent cations and elemental metal [12].

Due to this lower equilibrium concentration, metal cations get reduced/redeposit on the colder leg while dissolution continues on the hot leg [9]. It is reported that the solubility of Cr in FLiBe melt increased by 50% with the temperature increase from 600°C to 800°C. This increase in solubility was reported 150% in FLiNaK salts [34]. It can be concluded that the presence of temperature gradient can drive the corrosion as long as the colder section and the hotter section of the system are in electrical contact with each other and the ionic contact is made through the electrolyte in between.

2.6 Thermodynamic Landscape of Metal Fluoride Interactions

Corrosion of metals occurs through electrochemical reactions where the less noble anodic material is oxidized and the more noble cathodic material is reduced, forming a redox pair. When metals are exposed to environments such as air, water, or acids, this process typically results in the production of oxides or salts. In some cases, particularly with certain metal alloys, corrosion promotes the formation of dense, adherent oxide films. These protective oxides hinder the diffusion of oxidizing agents to the metal/oxide interface, thereby reducing reaction rates and passivating the surface. Such behavior is commonly observed in alloys with specific amounts of alloying elements like chromium or aluminum, which leads to the formation of stable oxides such as Cr_2O_3 and Al_2O_3 [12].

However, in case of fluoride salts, fluoride anion incorporates in oxide scales along anionic lattice paths. Consequently, corrosion resistance in molten fluoride environments cannot be achieved through alloy composition adjustments aimed at forming a stable, protective oxide layer. As a result, the corrosion resistance of the alloy in contact with fluoride salts necessitates an initial assessment of the redox potentials of the constituent elements in relation to the components of the salt [35]. It can be concluded that the fluoridation of the alloying elements and the formation of the metal fluorides play an important role in determining the thermodynamically driven dissolution of alloying elements [8, 35, 36].

In 1987, the National Aeronautics and Space Administration (NASA) conducted a study in which equilibrium concentrations of metal fluorides were calculated for the corresponding metals (M) in contact with LiF, NaF, and KF, considered individually [10]. The study revealed a consistent trend across all three fluoride salts, with the tendency of metals to form their respective fluorides increasing in the order: Ni < Co < Fe < Cr < Al. In a subsequent section of the report, the impact of water impurities was also investigated. It was found that the reaction of alkali fluorides with water generates HF gas by reaction 12. The dissolved HF can then react with the metal and cause serious corrosion problems by the formation of metal fluorides [10]. Importantly, the report did not address the generation of fluorine gas and explicitly noted the reduction of hydrogen protons [10]. In the NASA study, the heats of formation for various metal fluorides (derived from the reaction of metals with fluorine gas) were not explicitly utilized.

$$2AF(l) + H_2O(g) = M_2O(l) + 2HF(g) \qquad R\ 16$$

Part of the gas will dissolve in the melt by the reaction:

$$HF(g) = HF(l) \qquad R\ 17$$

$$xM + yHF = M_xF_y + \frac{y}{2}H_2 \qquad R\ 18$$

Olson et al. [8] calculated the Gibbs free energy of formation of different metal fluorides per molecule of fluorine gas. The Gibbs free energy of formation for all metal fluorides were calculated to be negative in this study with the energy values becoming more negative in the following order: Ni<Co<Fe<Cr<Al.

In their thermodynamic analysis, fluorine gas (F_2) was included in the reaction schemes, although it was not physically introduced into the system [8]. Calculations were done irrespective of the specific alkali fluoride salt used and the incorporation of F_2 led to the prediction that all metal fluorides would form spontaneously. These calculations were effective in terms of comparing the propensity of the formation of different metal fluorides. However, the negative Gibbs free energy in those calculations do not indicate which of the metal fluorides are stable in a specific environment (if at all).

For instance, formation of Mo and Ni enrichments have been reported, which indicate their better corrosion resistance of these elements to fluoride salt melts [10, 28, 31, 35]. The corrosion resistance seen in Ni and Mo rich precipitates was reported to be related to the relatively lower negative free energy of formation of molybdenum fluorides in comparison with other metal fluorides [28]. Also niobium has been reported to be selectively corroded [30].

The inclusion of fluorine gas in the highly referenced study by Olson et al. has created the confusion that fluorine gas exists in the system [8]. In another study, Olander et al. studied the redox state in the formation of metal fluorides and suggested that the redox condition is related to the chemical potential of the anion species [37]. The presence of impurities like HF or oxygen gas in an attempted non-oxidizing environment is ignored in this study. The anion species are considered to be elemental gases in their normal state, which would mean that the chemical potential can be defined in terms of partial pressure. Hence, in reaction 19, the X potential is defined in terms of the partial molar Gibbs free energy of a diatomic gas X_2, where X= O, F, Cl,…

$$MX_n + \frac{1}{2}X_2(g) = MX_{n+1} \quad where\ 0 \leq n \leq 4 \qquad R\ 19$$

$$\Delta G_{x_2} = RT ln\, p_{x_2} \qquad R\ 20$$

It is mentioned in the publication by Olander et al., that it is not necessary that the gaseous species of for example O_2 is physically present in the system, a metal and its oxide are mentioned to be in an enclosed system and yet exhibit a theoretical oxygen pressure [37]. For the molten fluoride salts, x_2 is considered to be fluorine gas and the redox condition is termed the fluorine potential:

$\Delta G = RT \ln p_{F_2}$ *R 21*

The formation of metal fluorides depends on the partial pressure of fluorine gas in this reaction. The stability of the metal fluorides is discussed to be based on the free energies derived from the equation above [31]. The difference in the free energy of the fluoride salt constituents and the fluorides of the alloying elements has been mentioned as the driving force for corrosion. This would mean that metals which their corresponding metal fluorides have a more negative free energy of formation are more prone to corrosion, because they are more likely to dissolve in the salt as a fluoride compound [28].

To investigate the formation of FeF_3 from fluorine gas, Zhou, Johnson and colleagues introduced F_2 directly into the system, thereby justifying its inclusion in the thermodynamic calculations [38, 39]. However, in the absence of active fluorine gas injection, the generation of F_2 from alkali fluorides upon interaction with oxygen or metal oxides or the alkali fluoride salt remains speculative. Though, corrosion in alkali fluoride salts under inert conditions has been extensively studied, with many works citing metal fluoride formation enthalpies while neglecting both the lack of fluorine gas introduction and the influence of redox-active impurities [9, 12, 33, 36, 40, 41].

Some investigations under oxidizing environments have linked corrosion in alkali fluoride salts to the generation of intermediate fluorine gas that recirculates within the system [13, 42]. These studies base their discussions on a mechanism, commonly referred to as “active oxidation” which was first proposed by Grabke et al. [43]. In the context of fluoride salts, active oxidation suggests that fluorine gas forms via interaction between condensed alkali fluorides and the oxide scale on the metal. In the presence of moisture, HF gas may be generated and subsequently oxidized to produce fluorine gas and water. As shown in figure 6, it is claimed in this mechanism that fluorine gas can diffuse through cracks in the oxide scale to the metal/oxide interface, where it reacts with the alloy to form metal fluorides. These metal fluorides are considered to be migrate towards the oxide/salt interface where the higher partial pressure of oxygen promotes their oxidation. As illustrated in figure 6, the formation of the metal oxide at the oxide/salt interface is supposed to be accompanied by the release of F_2 gas. The released fluorine gas is argued to act as a corrosion catalyst re-entering the oxide scale and repeat the same cycle of making metal fluorides at the metal/oxide interface. Although this mechanism has been predominantly explored for chloride salts [44, 45], it has also been applied to corrosion behavior in alkali fluoride salts [42].

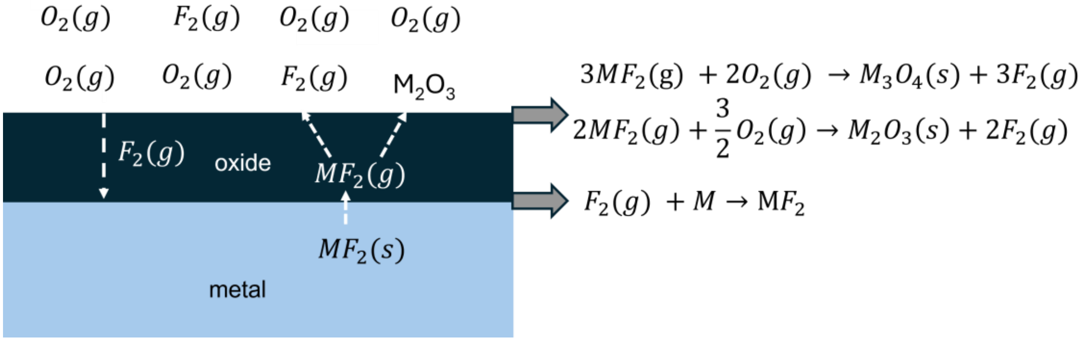

Figure 6) Schematic viewof the so-called "active oxidation" mechanism in fluoride corrosion.

The presence of metal fluorides/chlorides at the metal/oxide interface does not necessarily confirm the presence of fluorine/chlorine gas in the oxide scale. Hence, Folkeson et al. proposed another mechanism which does not involve gas phase transport through the scale and is instead coupled by the migration of anions and cations through the oxide scale [46]. This mechanism was suggested for alkali chloride salts, though, an extension of this theory to fluoride salts is discussed here.

Unlike the active oxidation mechanism in which the presence of HF is discussed to lead to the formation of fluorine gas, fluoride ions are generated in the electrochemical approach as shown in reaction 22. In this case cathodic current is provided by the reduction of oxygen and anodic current by the oxidation of the transition metals as alloying elements.

$$2HF(ads) + ½\, O_2(ads) + 2e^- \rightarrow H_2O(g) + 2F^-(ads) \qquad R\ 22$$

$$Me(s) \rightarrow Me^{n+} + ne^-$$

The second source for production of fluorine gas in active oxidation mechanism is discussed to be the oxidation of alkali fluoride salts. As shown in reaction 23, fluoride ion can be generated in this case.

$$2LiF + \frac{1}{2}O_2(g) + 2e^- \rightarrow Li_2O + 2F^- \qquad R\ 23$$

$$Me(s) \rightarrow Me^{n+} + ne^-$$

By applying ion diffusion mechanism, the fluoride ion would be expected to diffuse through the oxide grain boundaries or oxygen sublattice. The diffusion of monovalent halogenides is expected to be faster than the divalent oxygen ion [47]. The faster diffusion of the fluoride ion to the metal/oxide interface would then lead to the formation of metal fluorides. Discussions in the present study and the suggested mechanisms are based on the electrochemical approach.

However, the energetic values for the possibility of applying the active oxidation mechanism are calculated in table 4 in the discussion section.

2.7 Kröger-Vink notation

The systematic description of point defects in inorganic compounds, particularly oxides, necessitates a robust notation capable of accurately representing the defects and their associated charges under varying experimental conditions. In this context, the Kröger-Vink notation has been widely adopted, providing a comprehensive framework for articulating defect chemistry by denoting both the species involved and their lattice sites through subscripts. Deviations such as vacancies and interstitials are represented using symbols like V_O for oxygen vacancies and O_i for oxygen interstitials. We consider the formation of an oxygen vacancy by removing an oxygen atom from the crystal, if two electrons are localized at this empty site, the oxygen vacancy has two negative actual charges. Hence, the charge at this site is the same as in the perfect crystal and the oxygen vacancy then has zero effective charge. Crucially, Kröger-Vink notation incorporates the effective charge of defects relative to a perfect crystal, using superscripts to denote neutral (X), positively charged (·), or negatively charged (′) species, thereby reflecting their influence on the crystal's overall charge balance. For instance, singly and doubly charged oxygen vacancies are denoted as $V_{\dot{O}}$ and $V_{\ddot{O}}$ respectively, while cation vacancies can appear as V_M' and V_M''' depending on their ionization state compared to the nominal lattice site's charge [48]

3.Experimental Methods

3.1 Materials

Lithium fluoride (LiF, 97%) and sodium fluoride (NaF, 99%) were purchased from Thermo Scientific. The experiments were carried out at a temperature range of 50-600°C, which is below the melting point of both LiF (848°C) and NaF (993°C). Neither of the salts were molten at the working temperatures, however, the possibility of the formation of molten phases should be taken into account. Experiments in this study were carried out under oxidizing conditions (filtered air) hence, the salts were not purified in this study.

Inconel 625 sheet was selected for this study and was purchased from ThyssenKrupp VDM with the trademark NICROFER 6020 HMQ. The plate was hot rolled and heat treated at 1020°C. The nominal composition of this alloy can be found in Table 1. Inconel 625 strips ($350\times10\times3$ mm^3) were cut and polished to a 600-grit finish using a silicon carbide grinding band.

Table 1) Nominal alloy compositions (wt%) of the Inconel 625 provided by the supplier

Ni	Cr	Mo	Fe	Nb	Ti	Si	Others
balance	21.51	8.69	4.32	3.31	0.20	0.12	C 0.02

3.2 Sample preparation

Exposures in this study were partly carried out in a tube furnace which makes it possible to expose samples isothermally. In this case, coupons of Inconel 625 were cut into $3\times10\times15$ mm^3 size and immersed in the alkali fluoride salt in alumina crucibles. These coupons were automatically ground using Struers TegraPol-31 polishing machine in water using silicon carbide (SIC) paper grit size of 320 up to 1200 grit. This process was followed by polishing with diamond suspensions 3 and 1 mm until mirror-like surface was achieved. The samples were then degreased using acetone.

For the temperature gradient studies however, long strips of Inconel 625 were cut to be exposed over a range of temperatures. These strips were cut from a sheet into pieces of $350\times10\times3$ mm^3.

Since these strips were too long, it was not possible to polish them on the polishing machine used for the coupons, hence a Stenbergs NÄSSJÖ Tingströms grinding band was used in this case, which is illustrated in figure 7. The grinding band was not equipped with water and the samples were polished to a 600-grit finish in this case using silicon carbide bands.

Figure 7) grinding band used to polish the metal strips.

3.3 Furnaces

3.3.1 Isothermal Exposures

Considering the fact that there were isothermal and temperature gradient experiments carried out in this work, two different setups were used to make it possible to have samples immersed in the salt during the exposures. Part of the isothermal studies were carried out in a tube furnace at 600 ± 2 °C using an alumina tube of 35mm in diameter. As presented in figure 8, the samples were immersed in small alumina crucibles and the crucibles were placed in alumina boats to prevent possible contamination and exposure of the alumina tube to the alkali fluoride salts. These exposures were conducted under dry filtered air at a flow rate of 8 ml/min for different durations of 168-1000 hours.

Figure 8) schematic of the tube furnace used in isothermal exposures.

3.3.2 Temperature gradient exposures

To evaluate the effect of a temperature gradient on the corrosion behavior of Inconel 625, long strips of the alloy were exposed to alkali fluorides under a controlled gradient ranging from 50 °C to 600 °C. To maintain immersion of the metal samples in the alkali fluoride salts throughout the exposure period, a dedicated vertical setup was designed, as illustrated in figure 9a.

The samples were positioned inside alumina crucibles which are 500 mm in length, featuring a closed-end design. These crucibles had an internal diameter of 12 mm, providing a 2mm clearance around the 10mm wide metal strips. This configuration ensured complete exposure of the samples to the surrounding salt medium. To establish a stable thermal gradient along the crucible length, the crucibles were placed vertically within steel vessels, which not only supported the crucibles but also contributed to uniform heat conduction.

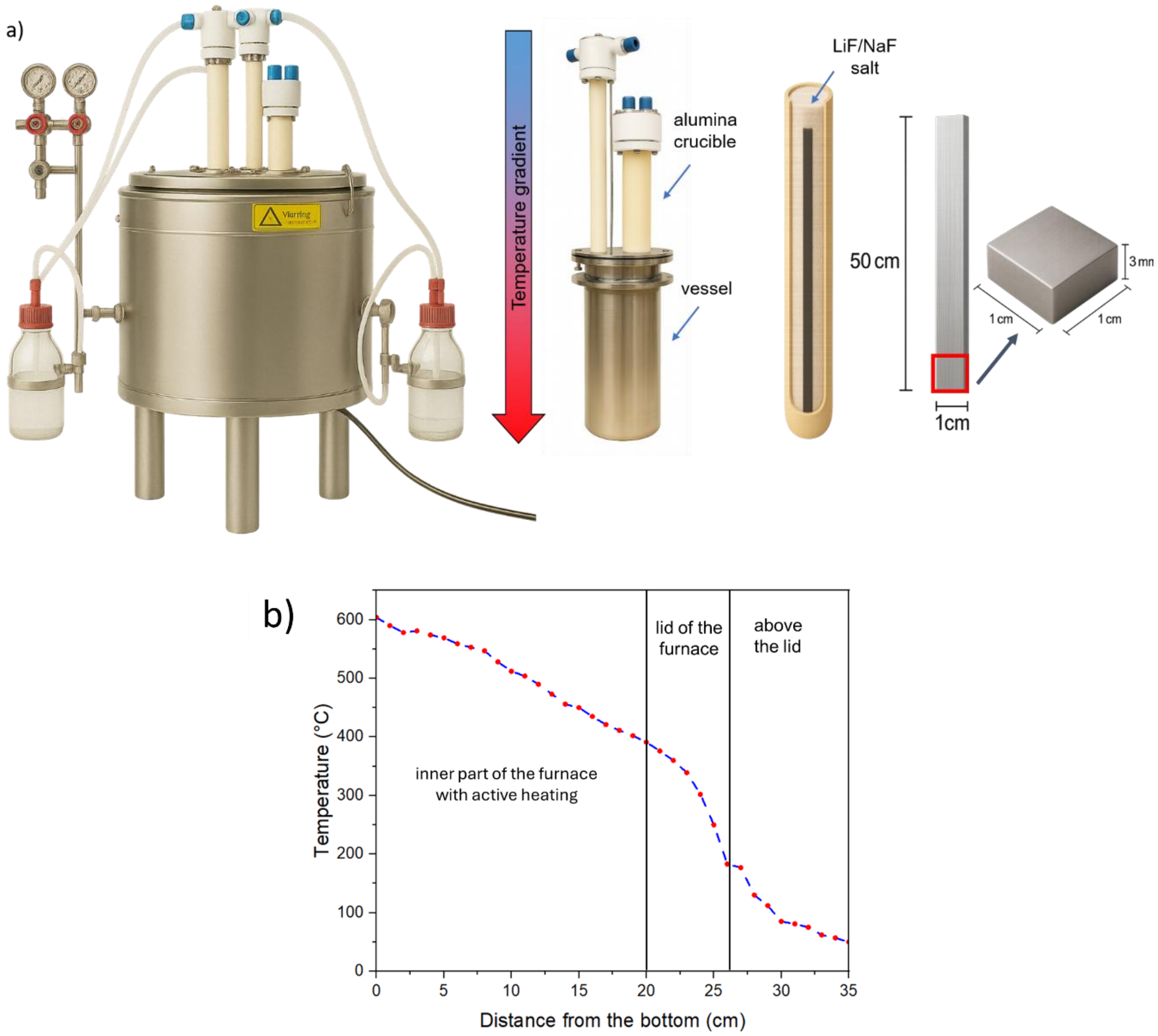

Figure 9) a) schematic of the vertical setup b) temperature gradient through the alumina crucible (highest temperature represents the bottom of the crucible where).

A continuous flow of filtered, dry air was introduced from the top of the alumina crucibles via a dedicated gas inlet, as depicted in figure 9a. This arrangement facilitated the creation of a controlled oxygen environment while enabling the establishment of the intended temperature gradient along the length of the crucible. The alkali fluorides employed did not melt at 600 °C and the permeability of oxygen through the solid salt column remained a key factor. Given that approximately 350 mm of the crucible was filled with salt, the partial pressure of oxygen at the bottom (corresponding to the highest temperature zone) was lower than the top.

The vertical exposure system was implemented using a Nobertherm Top 60 vertical furnace, which is loaded from the top and accommodates two steel vessels containing the alumina crucibles. The heating elements, located in the lower section of the furnace, provided active heating, ensuring that the highest temperatures were achieved in the lower regions of the crucibles. The temperature profile inside the crucibles was carefully calibrated, as presented in figure 9b. Three distinct regimes were identified: (i) from the bottom, up to approximately 200 mm, where the crucible was situated within the heated zone of the furnace, displaying an almost linear gradient from 600 °C to 400 °C due to the action of three active heating elements; (ii) the transition zone within the thick insulated furnace lid, constructed from refractory bricks, where the temperature declined more rapidly; and (iii) the upper section extending beyond the furnace body, where the crucible was exposed to ambient air, resulting in rapid cooling from 183 °C to 35 °C over a 100 mm distance.

3.4 Characterization and Analysis Techniques

3.4.1 Scanning Electron Microscopy

The scanning electron microscope (SEM) operates by scanning a finely focused electron beam over the surface of a sample in a regulated raster sequence to achieve magnification and imaging. This interaction produces various signals, notably backscattered and secondary electrons, which offer detailed insights into the specimen's topography and elemental composition [49].

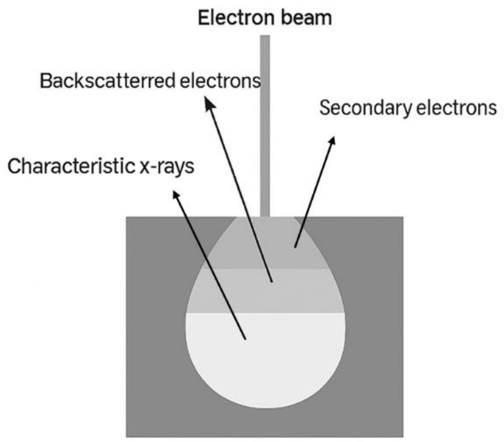

Figure 10) schematic illustration of the interaction volume and different signals produced in scanning electron microscope.

Secondary electrons:

The most commonly utilized signal in SEM is the secondary electron (SE) emission resulting from the interaction of the primary electron beam with the specimen. When the beam strikes the surface, loosely bound electrons are ejected; due to their low energy (typically 3–5 eV), secondary electrons escape only from a shallow region a few nanometers deep. This confinement provides precise localization of the beam and enables high-resolution topographic imaging. Secondary electrons are primarily employed to visualize surface texture and roughness [50].

BSE electrons:

Backscattered electron (BSE) imaging is another valuable SEM technique, providing both compositional and topographic information. BSEs are electrons that have undergone one or more elastic scattering events and escape the surface with energies exceeding 50 eV. Heavier elements, with higher atomic numbers, backscatter more electrons due to their greater nuclear charge, resulting in enhanced BSE signal intensity and enabling atomic number contrast. As BSEs originate from a deeper interaction volume than secondary electrons, their images exhibit lower lateral resolution [50].

3.4.2 Energy Dispersive X-ray Spectroscopy

Characteristic x-rays are produced when incident electrons eject inner-shell (K, L, or M) electrons from atoms in the specimen. An electron from a higher-energy shell then fills the vacancy, emitting a photon whose energy equals the difference between the two shells. These emitted x-rays have element-specific energies, typically ranging from hundreds to tens of thousands of electron volts, allowing for elemental identification and compositional analysis. Elements with higher atomic numbers exhibit more electronic transitions and produce higher-energy x-rays. By incorporating an x-ray detector, the SEM can measure these characteristic x-rays, enabling spatially resolved elemental identification and quantification across the sample surface [49].

The characteristic x-rays emitted from lithium under the electron beam are low energetic and do not reach the detector. In addition, most of the generated x-rays are absorbed by the sample itself. Hence, detection of lithium by a classical EDS detector is not possible [51]. In order to detect the possibility of the presence of lithium in LiF exposures, Time of Flight Secondary Ion Mass Spectroscopy (SIMS) was used.

3.4.3 Time of Flight Secondary Ion Mass Spectroscopy (TOF-SIMS)

In secondary ion mass spectrometry (SIMS), a focused beam of energetic primary ions is directed onto the sample surface under high or ultra-high vacuum conditions. The momentum transfer from these primary ions induces sputtering of surface atoms and molecules. As illustrated in figure 11, among the ejected species, some acquire a positive or negative charge and are referred to as secondary ions. These ions are extracted into an analyzer by means of a high-voltage potential, and their mass-to-charge ratios are determined based on their time-of-flight from the sample surface to the detector [52, 53].

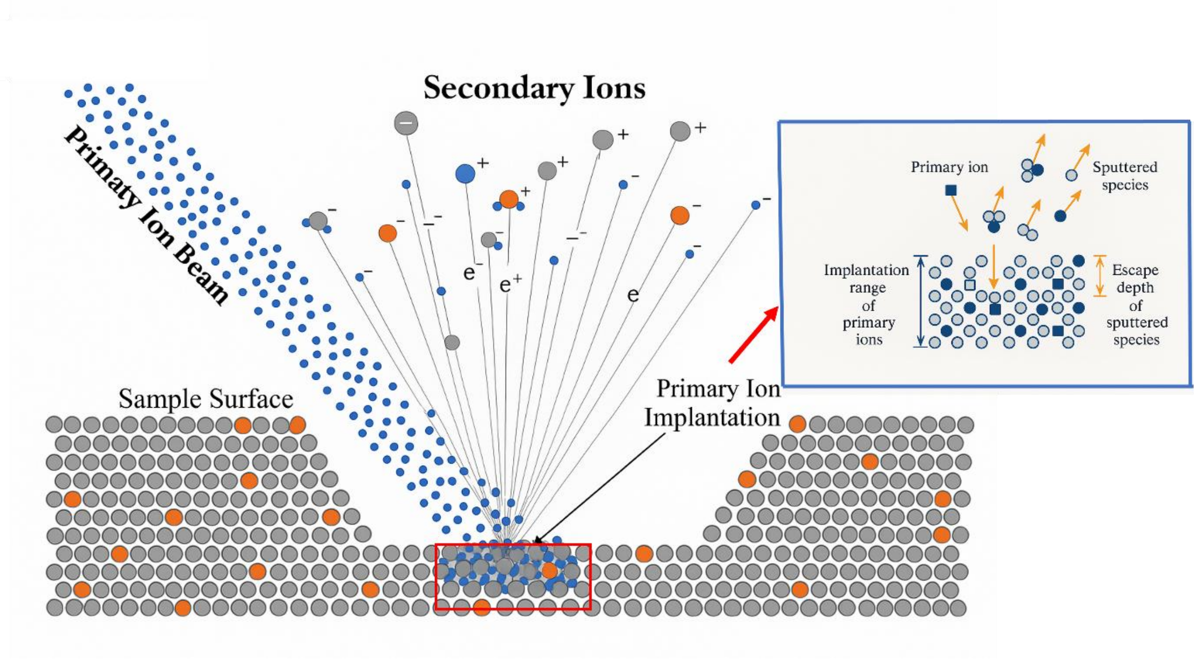

Figure 11) SIMS process, showing the penetration of the primary ion beam generating secondary ions of different charges inspired by [54].

The bombardment of a solid surface with a flux of energetic particles can result in the ejection of atomic and molecular species (a process known as sputtering). The ejected species may be monatomic, polyatomic, or multicomponent, and can exist in various charge states: positively charged (+), negatively charged (−), multiply charged (±p), or neutral (0) [52].

Sputtering of surfaces in the presence of electropositive species, such as with cesium primary ion beams, results in an enhanced generation of negative secondary ions. In contrast, the use of an oxygen primary ion beam significantly enhances the yield of positive secondary ions, resulting in strong measured ion signals. If an inert primary ion beam such as argon is employed, the intensity of the positive secondary ion signals will be 100 to 1000 times lower.

The bismuth or galium liquid metal ion gun (LMIG) is widely adopted as the standard ion beam for imaging, owing to its efficiency in enabling fast submicron imaging [52, 53].

A TOF-SIMS V system (ION-TOF, GmbH, Münster, Germany) was employed to analyze lithium ingress in LiF-exposed samples, utilizing a Bi_3^+ ion beam for imaging with 0.45 pA in spectrometry mode and 0.6 pA in fast-imaging mode. The ion beam was operated at 30 keV with an estimated beam focus of ~100 nm. Fast-imaging mode provided nominal mass resolution and an average primary ion dose of 8.11×10^{12} ions/cm². Data were processed using Surface Lab 7 software (Version 7.4, ION-TOF, GmbH). While spectrometry mode was used for reliable peak assignment, the high image resolution mode (fast imaging) was preferred for its enhanced spatial resolution, despite its lower mass resolution. This limitation was not critical, as the lithium-ion signal (m/z 7.13) did not interfere with other masses. Analyses targeting both electropositive and electronegative species enabled the simultaneous detection of lithium and fluoride. For the sample exposed over 168 hours, sputtering with oxygen and cesium ions was performed in positive and negative modes, respectively, at a dose of 9.2×10^{14} ions/cm². However, after 1000 hours of exposure, lithium and fluoride ingress were clearly observable without sputtering.

3.4.4 X-Ray Diffraction (XRD)

Bragg observed that x-ray diffraction behaves analogously to the reflection of waves from atomic planes within a crystal; however, this phenomenon occurs only at specific crystal orientations relative to the x-ray source and detector. Unlike conventional mirror reflection (where the angle of incidence equals the angle of reflection and is valid for all angles), x-ray reflection is restricted to instances where the conditions for constructive interference are satisfied as shown in figure 12.

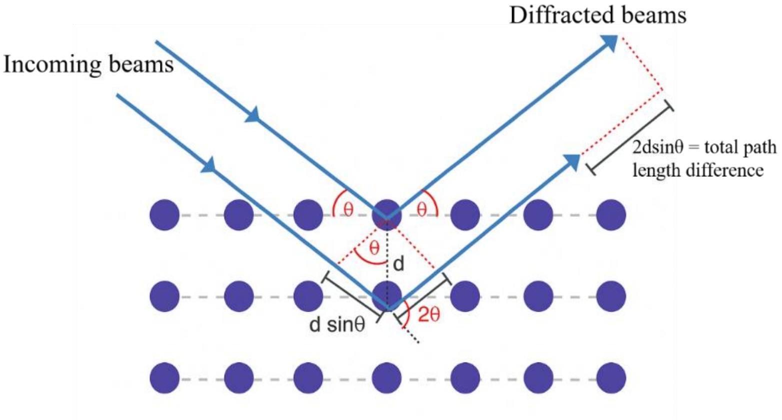

Figure 12) Geometrical illustration for diffraction from lattice planes.

For the reflected beams to emerge as a coherent beam of appreciable intensity, they must constructively interfere (that is, arrive in phase with one another). Constructive interference occurs when the path length difference between the interfering beams corresponds to an integral multiple of the wavelength [55]. This path length difference must equal an integer number n of wavelengths. If the x-ray wavelength is denoted by λ, then the condition for constructive interference is expressed by the Bragg equation:

$$n\lambda = 2d_{\mathrm{hkl}}\sin\theta_{\mathrm{hkl}}$$

This equation relates the interplanar spacing d_{hkl} to the specific Bragg angle θ_{hkl} at which reflections from the corresponding set of crystal planes are observed [55, 56].

4.Results

4.1 Corrosion in LiF Salt (600 °C)

A part of this study was conducted to see the possible effects of having a temperature gradient in the system. Hence, three different scenarios were designed and studied in LiF exposures to distinguish the possible effects of having a temperature gradient in the system. Parallel isothermal exposures have been carried out to compare the results with the temperature gradient. In order to see if exposures in the vertical setup provides a different condition in comparison with those in the tube furnace, an isothermal exposure was carried out also in the vertical setup. Three different scenarios are defined this way, which are illustrated in the figure 13:

Figure 13) The three different exposures in LiF exposures scenario 1) temperature gradient exposure scenario 2) isothermal exposure in the vertical setup scenario 3) isothermal exposure in the tube furnace.

4.1.1 Thermal Gradient Exposure (Scenario 1)

As outlined in the literature review, the presence of a temperature gradient is recognized as a contributing factor to high-temperature corrosion. Given the existence of such gradients in various industrial applications, including nuclear reactors and battery recycling processes, this phenomenon is partly examined in the present study.

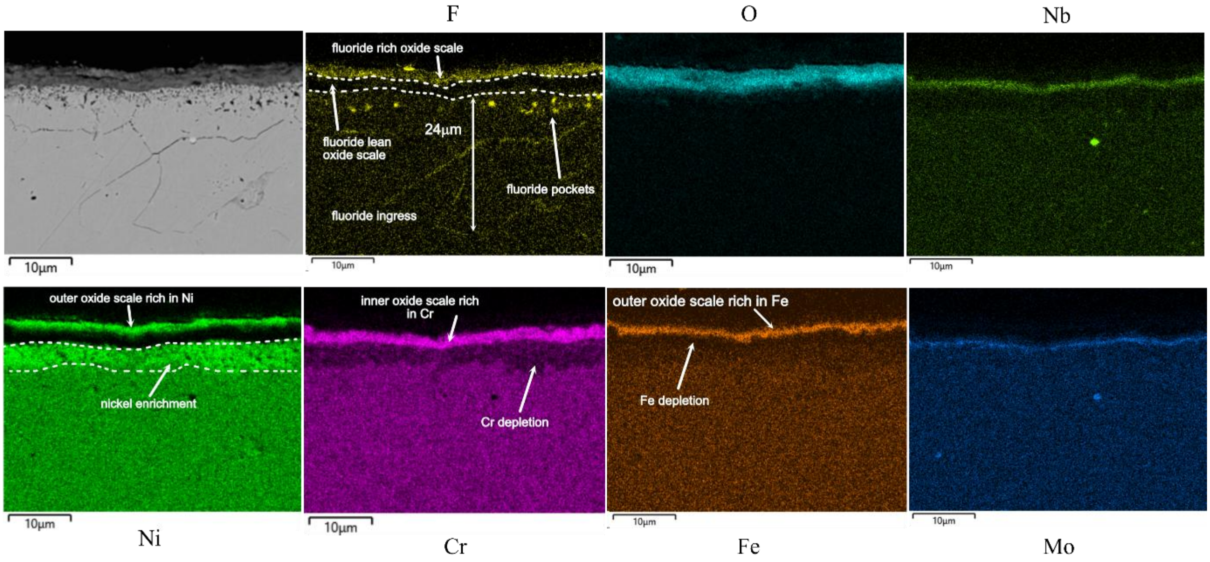

Figure 14) BSE and EDX elemental maps of the sample exposed in scenario 1 after 168 hours of exposure.

A strip of Inconel 625 was exposed to a temperature gradient ranging from 50 °C to 600 °C. A section of the strip exposed to 600 °C was cut and prepared as a coupon for analysis. The cross section of the sample, exposed for 168 hours, was examined using a scanning electron microscope. Backscattered electron image in figure 14 revealed pocket formation at the metal/oxide interface and intergranular attack extending into the metal to the depth of up to 24 µm. Energy-dispersive X-ray spectroscopy (EDS) mapping indicated that the pockets beneath the oxide scale were filled with fluoride, which had diffused into the metal along the grain boundaries via the intergranular attack. In contrast, oxygen remained confined within the oxide scale and did not penetrate the grain boundaries as readily as fluoride. EDS analysis also revealed a distinct chromium depletion zone beneath the oxide scale, and a less pronounced depletion zone for iron. Notably, nickel showed enrichment in the metal beneath the oxide scale, including in and around the fluoride pockets.

Fluoride penetration was expected to promote the formation of metal fluorides and to cause localized enrichment of specific alloying elements within the intergranular attack zones.

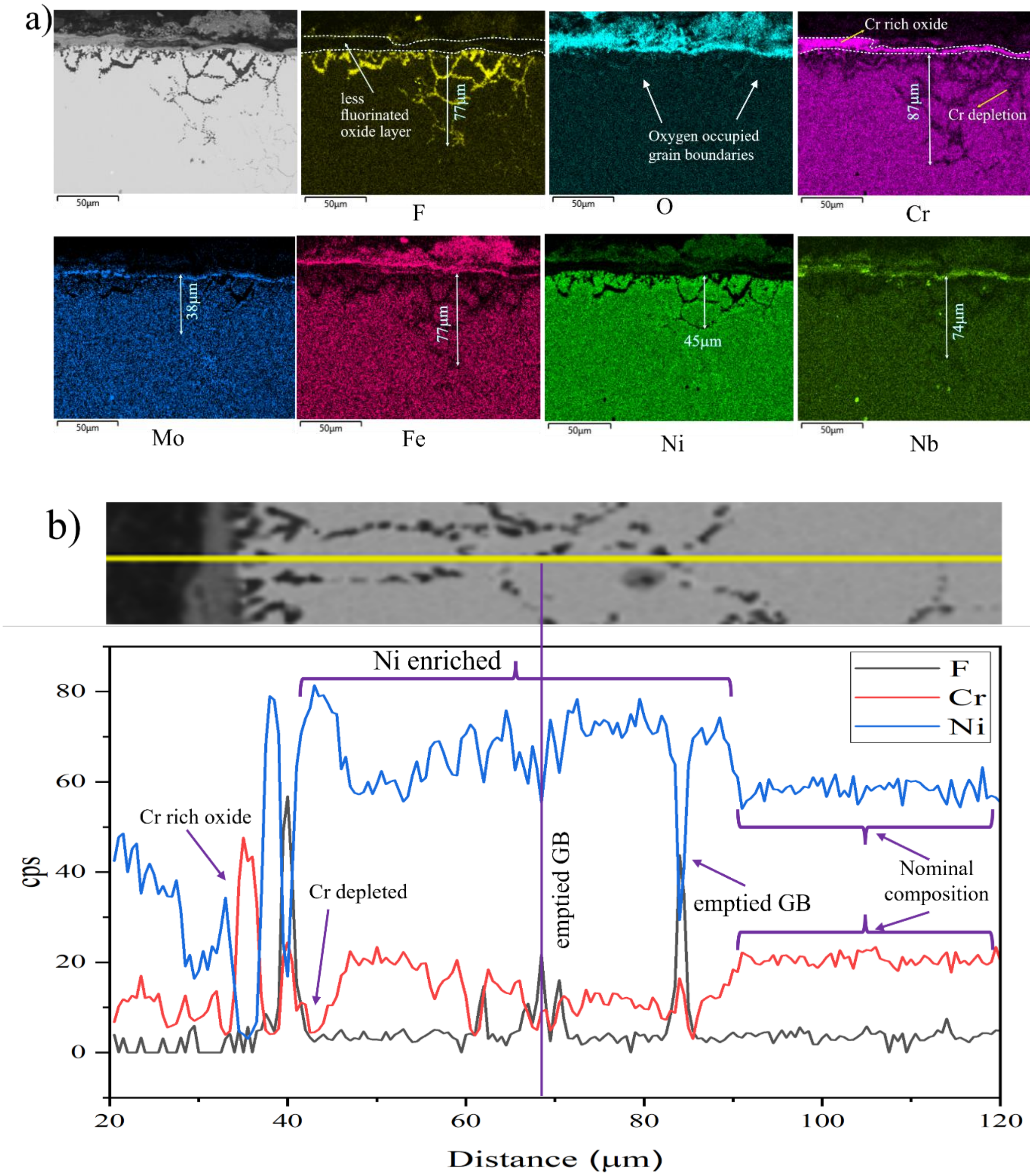

Figure 15) one line scan separated into two sections a) showing F, Mo and Ni, while b) showing Cr, F, Fe and Nb.

EDS analysis was also conducted on the sample exposed to a temperature gradient after 1000 hours of exposure. As shown in Figure 15a, fluoride penetrated the grain boundaries of the alloy, reaching a depth of 77 µm. A comparison of EDS results after 168 and 1000 hours indicates that, with prolonged exposure, oxygen begins to diffuse into the metal grain boundaries as well. The data further reveal that Cr is depleted not only from the grain boundaries but also from within the grains. Except for the larger grains where bulk diffusion of Cr takes longer, small grains have been exhausted and depleted from Cr and to a large extent from Nb and Fe. After 1000 hours of exposure, the upper grain boundaries are exhausted and emptied from Mo and Ni as well. In the Ni elemental map, the relatively high Ni content in the alloy makes these changes more discernible: Ni depletion is observed along the grain boundaries, while enrichment is evident in the lower grain boundaries and within the upper grains. The inner Cr rich oxide scale and the outer Fe and Ni rich oxide scale continue to be present.

To determine whether the alloying element concentrations differ between grain boundaries and grain interiors, EDS line scan analysis was performed from the metal/oxide interface to the bulk of the alloy, encompassing both grains and grain boundaries. Ni enrichment can be seen from the metal/oxide interface in figure 15b to 50µm deeper, where counts per second for Ni decrease to the nominal composition of the alloy. This enrichment within the upper grains results primarily from the depletion of other alloying elements, particularly Cr. The data reveal that Cr is depleted in the fluoride-rich grain boundaries, while Ni remains undepleted and shows increased counts per second. This is also evident in the clearly Cr-depleted grain boundaries. However, in certain smaller grains with wide-open grain boundaries, complete depletion of both Ni and Cr is observed.

The observed elemental responses to fluoride at the grain boundaries suggest that chromium, iron, and niobium are likely to form corresponding metal fluorides upon interaction with fluoride. In contrast, nickel and molybdenum are not expected to form their respective metal fluorides in contact with fluoride, as they remain enriched at the grain boundaries without evidence of depletion.

In order to investigate the oxide scale more, a higher magnification image was taken from the oxide scale together with the EDS maps, which can be seen in figure 16. The phases seen as layers in EDS results were matched with XRD results from scenario 1 shown in figure 19.

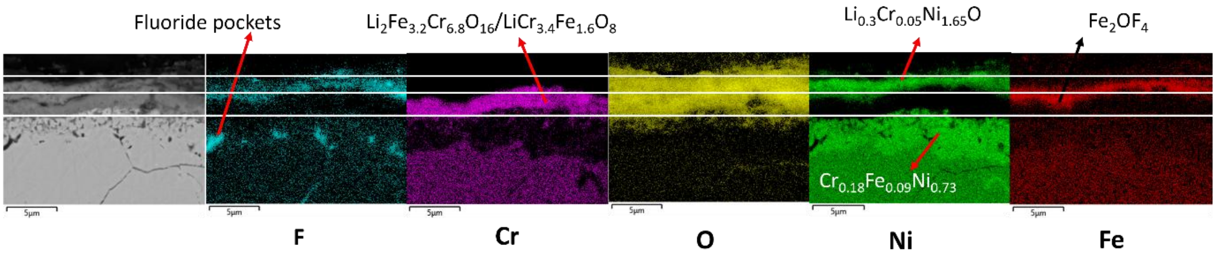

Figure 16) BSE image and EDX elemental maps of the sample exposed in scenario 1 condition after 168 hours.

The EDS maps showed a layered structure for the oxide scale. The inner part of the oxide scale comprised a Cr rich oxide scale and the upper part was an iron and nickel rich oxide. Due to the low atomic number of lithium and consecutively the low energy x-rays generated, it was not possible to detect lithium via EDS. However, XRD measurements showed the participation of lithium in the oxide scale. SIMS analysis was also done in order to see if lithium diffuses into the metal as well or not.

4.1.2 Isolated Coupon under Salt Column (Vertical Furnace, Scenario 2)

To draw conclusions on the effect of temperature gradient, it was necessary to expose a single coupon under the condition which the setup, the amount of salt and oxygen available are similar to scenario 1. To make this comparison, scenario 2 in figure 13 was experimented, where a coupon sample was also exposed to LiF in the vertical setup. To simulate oxygen access, the coupon was placed in an elongated alumina crucible, which was completely filled with LiF salt. This sample was isolated from any extended strip and lacked electrical conductivity to a longer conductive metallic segment. Given that the sample was exposed in the vertical setup under oxygen partial pressure conditions comparable to scenario 1, the influence of electrical conductivity along an extended strip of Inconel 625 can be evaluated. The extent of intergranular attack and the characteristics of the oxide scale may provide insights into the role of the temperature gradient. Backscatter electron images together with elemental analysis in figure 17 showed that the depth of intergranular attack in this case was 17μm, which is lower than that observed in scenario 1. Chromium depletion in this sample was comparatively limited, occurring primarily along the grain boundaries and within the immediate intragranular regions adjacent to those boundaries. The iron elemental map exhibited a depletion pattern analogous to that of chromium, confined to the regions immediately adjacent to the grain boundaries; however, because the alloy contains less iron, this depletion was less pronounced than the chromium depletion. The nickel map revealed enrichment adjacent to the intergranular attack, which was in agreement with the line-scan results obtained in scenario 1. A bilayer oxide scale comprising an inner Cr-rich layer and an outer Ni and Fe rich layer was also identified. This scale measured approximately 7 μm in thickness, comparable to that of the specimen exposed to the temperature gradient.

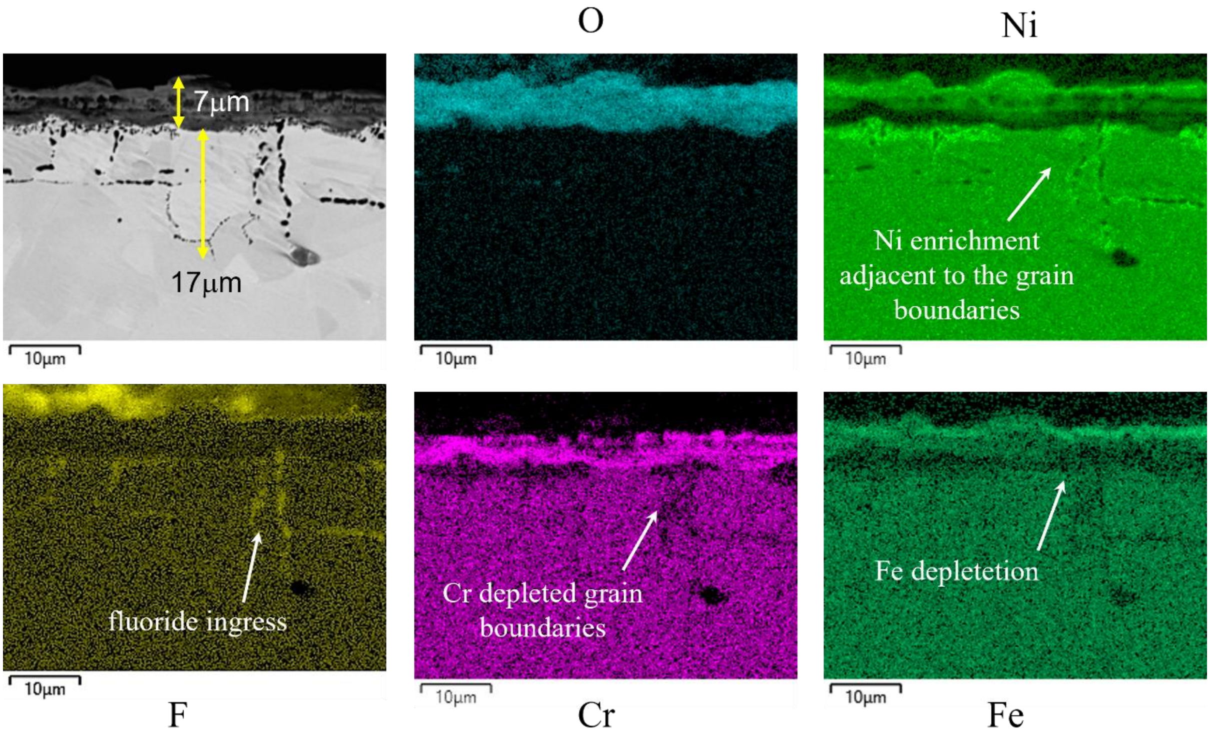

Figure 17) BSE image and EDX elemental maps of the sample exposed in scenario 2 (isothermal condition in the vertical furnace) after 168 hours.

Both scenarios 1 and 2 were conducted in the vertical furnace, where filtered air had to permeate the granular, solid salt to reach the sample positioned beneath the elongated crucible. The presence of a temperature gradient along a continuous Inconel 625 strip (scenario 1), resulted in more severe corrosion, underscoring the role of thermal gradients in exacerbating the corrosion process.

An isothermal exposure conducted in a tube furnace can eliminate the effect of having a temperature gradient but may involve elevated oxygen partial pressures. While the absence of a temperature gradient in scenario 2 is expected to mitigate corrosion severity, increased oxygen access could have an opposing effect. Consequently, the design of an experiment to isolate and compare the effect of not having a thermal gradient but more oxygen access is of particular interest. To assess the influence of salt quantity and oxygen partial pressure on the corrosion behavior of Inconel 625, corresponding isothermal exposure tests were conducted in a tube furnace.

4.1.3 Isothermal Coupon Exposure (Tube Furnace, Scenario 3)

The backscattered electron image of the sample cross-section revealed a more pronounced intergranular attack. In this case, the intergranular attack was more pronounced and extended continuously along the horizontal direction. Due to the fluoride-filled nature of the attacked regions, a higher fluoride ingress was observed. The oxide scale exhibited significant heterogeneity in thickness; in some areas, oxide protrusions reached up to 28µm, while in others, they were as shallow as 5µm. This oxide scale was highly defect-rich and non-protective. The elevated defect density facilitated the diffusion of both oxygen and fluoride through the scale, ultimately resulting in increased fluoride ingress and accumulation along the grain boundaries of the metal. As can be seen in the oxygen map in figure 18, oxygen diffusion has not stopped at the oxide scale and continues to the upper part of the attack into the metal.

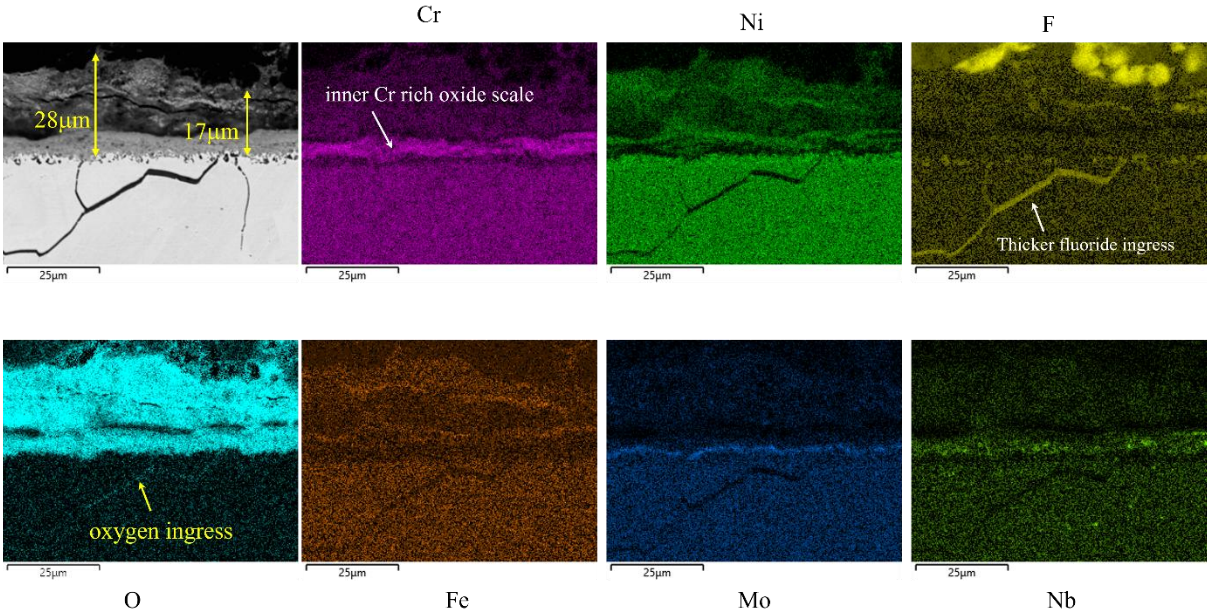

Figure 18) BSE image and EDX elemental maps of the sample exposed in scenario 3 (isothermal condition in the tube furnace) after 168 hours.

The oxide scale in scenario 3 (coupon in horizontal furnace) was very non uniform in its thickness. At some spots it was as thin as 5µm and at some others as thick as 28 µm. The higher fluoride ingress in this sample was eloquent of the less protectivity of the oxide scale against. The oxide scale in this case was slightly different from the two other cases where an outer iron rich oxide scale was seen. In this case, an inner chromium rich oxide scale was visible, but iron and nickel rich scales showed up both in the upper and the inner layer oxide scale.

The inner part of the scale which is chromium rich turns out to be more uniform in the BSE images as well. Unlike the two other scenarios, there was not much chromium depletion and nickel enrichment seen in and around the grain boundaries. In scenarios 2 and 3 however, an outer iron and nickel rich oxide scale was seen together with an inner chromium rich scale.

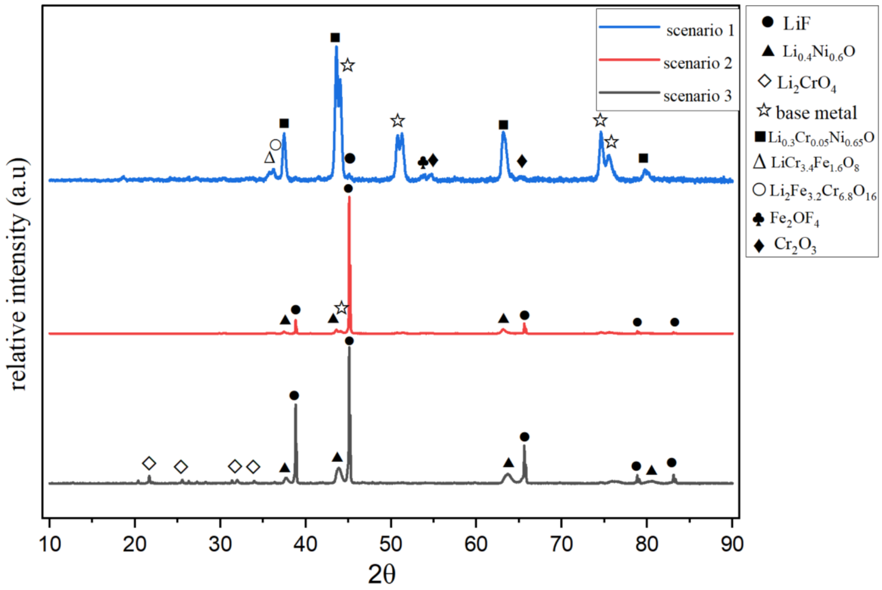

Figure 19) XRD patterns of the samples exposed in 3 different experimental conditions.

XRD analysis confirmed the formation of lithium chromates in scenario 3 (the horizontal furnace exposure). The formation of lithium chromates play an important role in the degradation mechanism. These alkali chromates can be the main cause of chromium consumption and would possibly interact with the salt mixture to form eutectic melts.

The presence of lithium chromate in scenario 3 implies either the disruption of a protective chromia layer or hindering its formation from the beginning. This disruption can happen by consumption of chromium from the bulk and/interaction of the scale with the salt mixture and oxygen, forming eutectic melts [57].

Considering that the samples were never peroxidized, the prior formation of a chromia scale is under question. It cannot be firmly concluded that the lithium fluoride salt breaks the chromia scale down and consumes it to form the lithium chromate. It is also possible that Cr from the bulk of the alloy is directly converted to lithium chromate through the following reaction:

$$Cr + LiF + O_2 \rightarrow \frac{1}{2}CrF_2 + \frac{1}{2}Li_2CrO_4 \qquad R\ 24$$

Or if we consider having humidity as impurity in our system:

$$Cr + 2LiF + H_2O + \frac{3}{2}O_2 \rightarrow Li_2CrO_4 + 2HF \qquad R\ 25$$

EDS results in all scenarios showed that the inner chromium rich oxide scale in all scenarios partly overlapped with iron or nickel. In a previous study in oxidation conditions on alloy 625, a 19nm thick Cr_2O_3 scale was detected in an investigation with Auger electrons [58]. Diffraction peaks in XRD results for scenario 1 were partly in line with Cr_2O_3, however, the mechanism behind the layered oxide scale is not considered breakaway. The oxide layer in none of the scenarios including scenario 1 showed protective features. Considering how thin the chromia scale detected in the study by Norling et al. was and the fact that samples were not peroxidized before exposure in our study, lithium is considered to react to the oxide scale since the beginning. The starting point of the corrosion attack in all cases in LiF corrosion is by the diffusion of fluoride into the alloy and making fluoride pockets. These fluoride pockets widen over time and more fluoride enters the bulk of the alloy. The corrosion layer grows both towards the LiF deposit and inwards.

The very defect rich and non-homogeneous upper scale in scenario 3 together with the depletion zone which is not as deep as the one in scenario 1, implies that the formation of eutectics in this case outweighs the consumption of chromium.

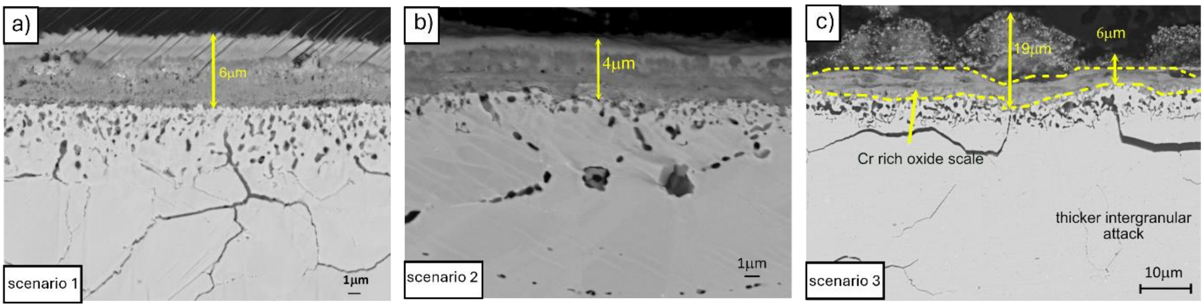

Figure 20) BSE image of the samples exposed for 168 hours in exposure condition a) scenario 1 b) scenario 2 c) scenario 3.

The probability of the formation of low melting mixtures should also be considered. Although the presence of niobium in alloy 625 is relatively low, NbF_5 has a melting point of 79°C, which makes it a low melting point corrosion product. The interaction between LiF salt, oxides and metal fluorides can lead to the formation of low melting point eutectic compounds. Although thermodynamic data is not available between all compounds which are possible to form, the phase diagram in figure 21 shows the lowest eutectic temperature calculated via Factsage. The first molten phase in this diagram shows up at 560°C. Considering that the alloy consists of more chromium than niobium, this eutectic can play an important role in making a non-protective oxide scale.

Figure 19 demonstrates that no chromate phases were detected by XRD in either scenario 1 or scenario 2. As illustrated in figure 20, the oxide scales formed in these two scenarios are markedly more compact and exhibit a more uniform thickness than the scale observed in scenario 3. The oxide scale in scenario 1 was more defect rich which led to the formation of more fluoride pockets underneath the oxide scale and deeper fluoride ingress via the intergranular attack.

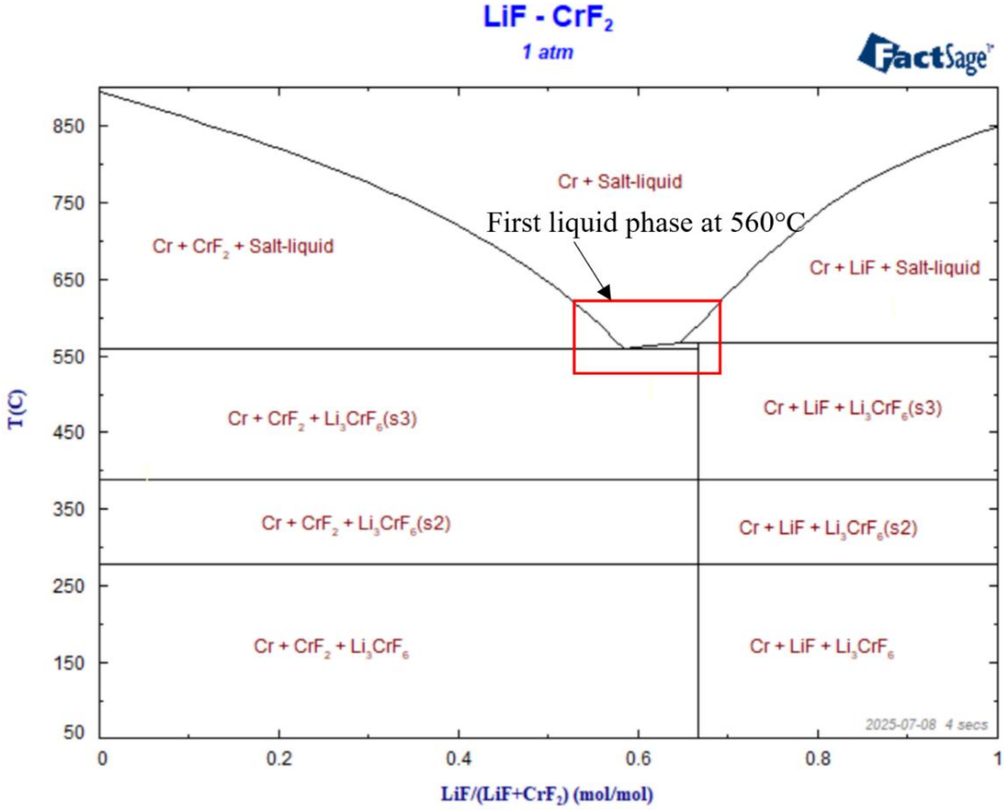

Figure 21) Phase diagram of the LiF–CrF$_2$ binary system at 1 atm and a temperature range of 50-900°C.

4.2 Tracking Lithium at Metal Grain Boundaries

XRD analysis confirmed that the oxide scales in LiF exposures were lithiated; however, lithium is too light of an element to be detected by EDS analysis. Hence, using a method in which the behavior of lithium can be tracked was of interest. EDS results in different scenarios (figures 14, 17 and 18) showed that the intergranular attack into the metal is filled with fluoride. Lithium as a positive ion is not expected to diffuse into the metal grain boundaries, however, a possibility was considered depending on how long the exposure was run. Hence, SIMS analysis was performed on the cross sections of samples exposed to a temperature gradient (scenario 1) after 168 hours and 1000 hours to assess the temporal evolution of lithium-ion diffusion.

SIMS results after 168 hours of exposure revealed fluoride diffusion along grain boundaries and into the pockets located beneath the metal/oxide interface. In contrast, as can be seen in figure 22a, lithium was detected in the oxide scale and salt residue, where its signal was markedly stronger than that of fluoride. Lithium map (figure 22a) indicated lithium-ion presence confined to the pockets at the metal/oxide interface. Although faint lithium signals were also detected below these pockets, they were at noise level and likely attributable to sample preparation artifacts (possibly smearing lithium from the interface on adjacent grain boundaries and grains). The low fluoride concentration in the salt residue, compared with that of lithium, suggests ionic separation within the salt. Fluoride ions, having dissociated from lithium, migrated into metal grain boundaries, forming metal fluorides. Notably, TOF-SIMS in negative mode showed fluoride (figure 22b) penetration along grain boundaries reaching depths of up to 16 μm after 168 bours of exposure.

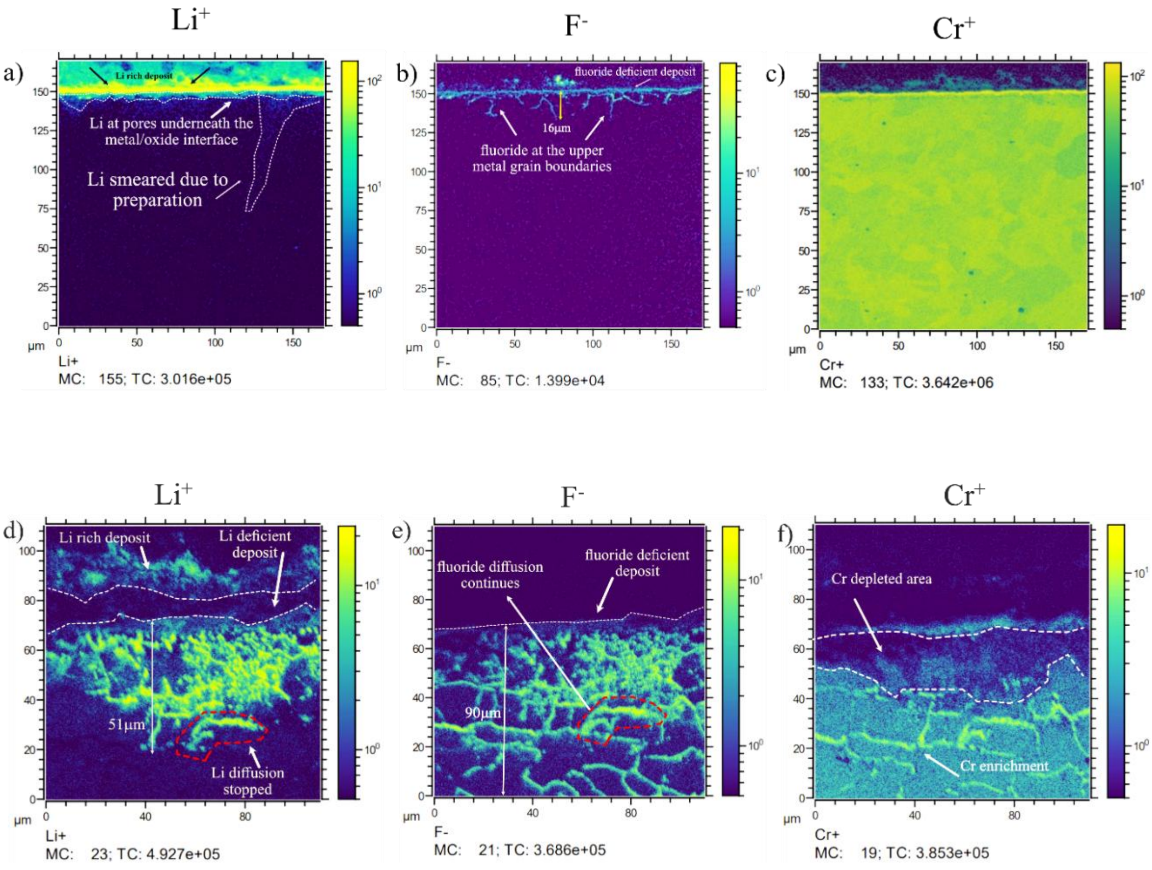

Figure 22) TOF-SIMS analysis on samples exposed to LiF a, b, c) after 168 hours d, e, f) after 1000 hours.

SIMS analysis was also carried out on a sample which was exposed for 1000 hours (figures 22d, e, f). Results after long exposures showed that fluoride ingress into the sample did not stop after 74μm and fluoride continued to diffuse deeper. The map for lithium however (figure 22d), shows that lithium has diffused into the grain boundaries of the metal as well, though stopped after 56μm. The difference in the depth of diffusion for lithium and fluoride into the metal confirms once more that they do not diffuse together, but separately. TOF-SIMS results from exposures at 600°C both after 168 hours and 1000 hours show lithium enrichment also in the oxide/salt interface. However, no fluoride enrichment is seen at the oxide/salt interface neither after 168 hours nor 1000 hours of exposure. These observations underline the fact that lithium and fluoride do not diffuse into the grain boundaries together and it is only fluoride which diffuses along the metal grain boundaries after 168 hours. A comparison between the lithium and the chromium map shows that lithium has diffused into the grain boundaries where Cr has been depleted and has stopped its diffusion once Cr enrichment is visible in the grain boundaries lying deeper in the alloy.

4.3 Corrosion in NaF Salt (600 °C, Thermal Gradient)

NaF is as well part of the FLiNaK salts and also with the advent of Na ion batteries is of interest in battery recycling industry. NaF has a melting point of 993°C and the exposure temperature which is 600°C is lower than its melting point. The comparison of results between LiF and NaF corrosion can clarify the effect of the salt on the corrosion mechanism.

The effect of having a temperature gradient on an alloy strip of which coupons at distinct temperature regions were cut for post exposure analysis was already compared with isothermal exposures in case of LiF salt. Hence, in the NaF studies we have focused on the mechanism of corrosion and the sample which is investigated was exposed to 600°C as a part of a temperature gradient.

In NaF exposures however, the corrosion behavior of Inconel 625 was completely different. No intergranular attack and porosities were seen into the metal or at the metal/oxide interface. The absence of the intergranular attack and porosities already implied that metal fluorides had not formed in such exposure. However, the absence of an intergranular attack did not necessarily imply a less corrosive environment for the alloy. Significant oxide formation and spallation was recognized after 1000 hours of exposure, which led to one-third of the sample thickness (1mm) being lost. This corresponds to an estimated mass loss of ~263 mg/cm², indicating that NaF is significantly more corrosive than LiF, where no significant thickness loss was observed. The oxide scale thickness shown in figure 23 is 123 µm, representing only the residual, non-adherent portion after spallation. As depicted in figure 23, no intergranular corrosion was observed in Inconel 625 even after 1000 hours. Sodium and fluoride were overlapping within the oxide scale but were not detected as crystalline phases by XRD. The oxide scale exhibits two distinct morphologies: a lower and compact layer of Mo, Na, and F rich region, and an upper granular structure containing Cr, Fe, and Ni. The upper layer comprises Fe, Ni, and Cr enriched islands embedded in a porous matrix rich in sodium and fluoride. These salt-rich regions do not coincide with areas of metallic enrichment, suggesting the absence of mixed oxide formation involving metal cations and salt components.

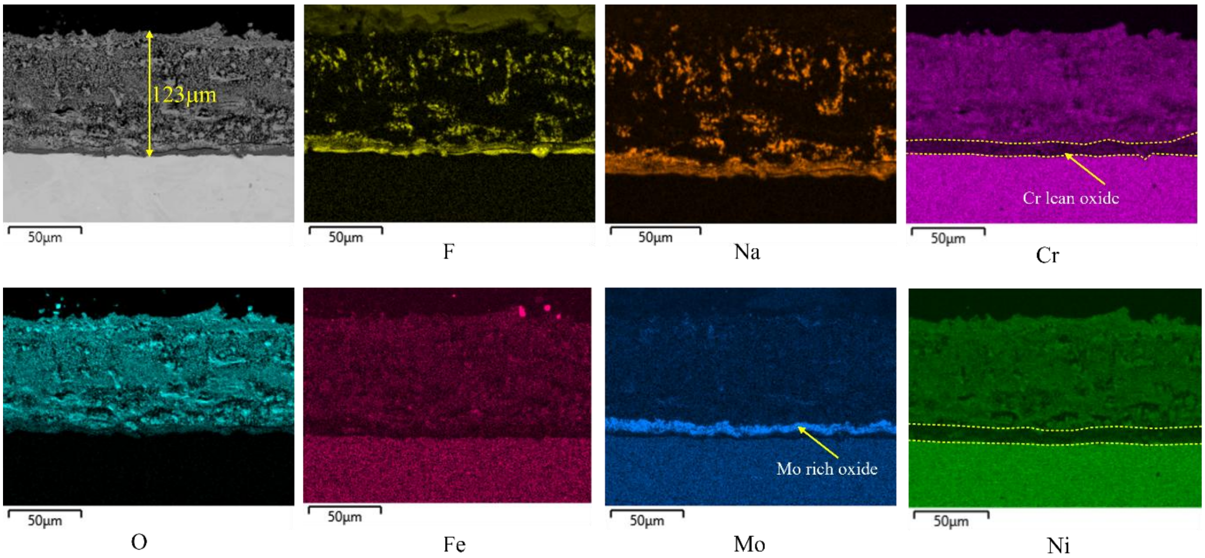

Figure 23) EDX map of Inconel 625 exposed to NaF for 1000 hours in oxidizing condition.

The EDS image in figure 23, shows enrichment of Mo and Na on the lower part of the oxide scale, but to analyze the oxide layer with more details, figure 24 was acquired at a higher magnification. Adjacent to the metal, between the metal and the oxide layer, there was a layer which showed up darker in the backscatter image. The lower part of the oxide scale on top of this layer, which was rich in Mo and Na. Consisting of the heavy element of Mo, this layer was detected brighter in backscatter images in comparison with the Na and F rich layer underneath. The structure of the oxide layer in figure 24 was very porous, with islands of iron, chromium and iron oxide. The contrast in the whole oxide layer showed sodium fluoride as darker porous regions and nickel oxide as the brighter spots in between. Sodium and fluoride did not overlap metal oxide islands which were detected in different parts of the oxide.

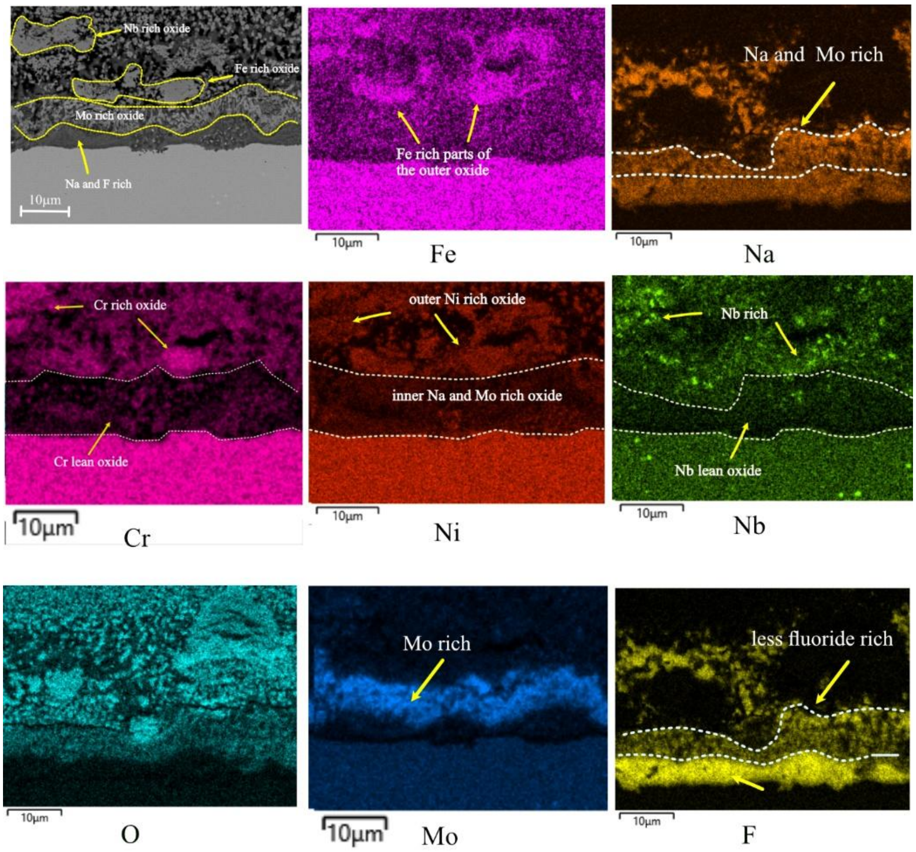

Figure 24) The lower part of the oxide scale in Inconel 625 sample exposed to NaF for 1000 hours.

Figure 25 shows the XRD analysis conducted on the sample exposed to NaF for 1000 hours. As shown in back scatter electron images, the oxide scale in this case was 123µm thick, which made it less probable to detect the underlying metal. The most intense diffraction signals in the oxide scale were identified as both $Cr_{0.3}Ni_{0.7}O_{0.65}$ and NiO. Based on EDS results, the oxide scale was rich in Ni but contained Cr as well. Hence, it is expected that a share of Cr would be detected in the oxide scale as well. This was in line with EDS maps where enrichment of Cr and Ni was seen. $Cr_{0.3}Ni_{0.7}O_{0.65}$ has a rock salt structure where cationic sites are shared by Cr and Ni (30% and 70% respectively).

As expected, Na and fluoride did not incorporate into the oxide scale. The islands of NaF in the oxide scale were not crystalline and there were no XRD patterns representative of these phases. At the lower part of the oxide scale however, enrichments of Na, Mo and F were seen in EDS maps, which meant that molybdenum oxyfluoride was the most stable metal oxyfluoride among other alloying elements. Diffraction signals for $Na_3MoO_3F_3$ were detected in the XRD analysis which can be representative of this Na, Mo oxyfluoride at the lower part of the oxide scale.

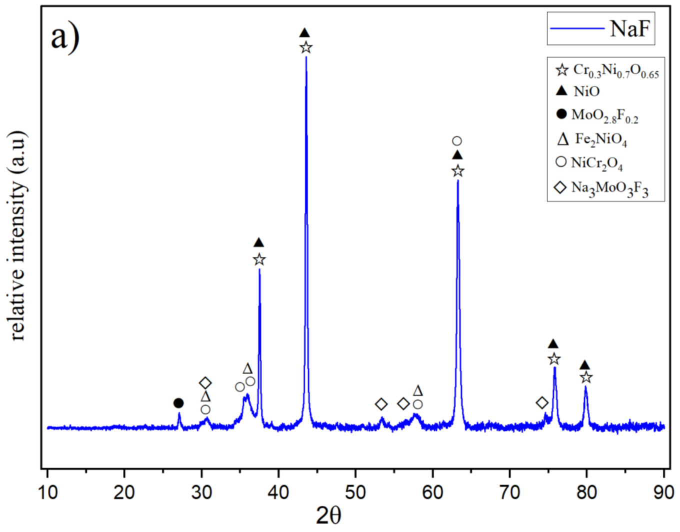

Figure 25) XRD pattern of the sample exposed to NaF in gradient condition after 1000 hours.

4.4 Thermodynamic Inspection of Metal Fluoride Formation in LiF and NaF exposures

There was a significant difference in corrosion behavior of alloy 625 in contact with LiF and NaF. The absence of intergranular attack in NaF exposures made the motivation to check and compare the stability of transition metal fluorides in both cases. To do so, reaction 26 was used to inspect different alloying elements for their spontaneity to form transition metal fluorides. Figure 26 illustrates the energy values for the formation of different transition metal fluorides from their corresponding metal in contact with oxygen and LiF/NaF. As can be seen in figure 26a, none of the transition metal fluorides show spontaneous formation when their corresponding metal reacts to oxygen and NaF. This is while FeF_2, CrF_2, CrF_3 and NbF_5 show stability when Cr, Fe and Nb react to oxygen and LiF (figure 26b). The depletion zone for Cr, Fe and Nb in LiF exposures in EDS results in figure 14, is in line with these elements forming stable metal fluorides with LiF. Also, the nickel enrichment at the metal/oxide interface and underneath the oxide is in line with nickel fluoride not being stable.

$$M + nAF + \frac{n}{2} O_2 \rightarrow MF_n + \frac{n}{2} A_2O \ (A = Li, Na), M = transition\ metal \quad R\ 26$$

According to figure 26a, none of the reaction energies for AF being NaF is showing spontaneity. This is also in line with the absence of any observable intergranular attack and lack of fluoride ingress into the alloy when in contact with NaF.

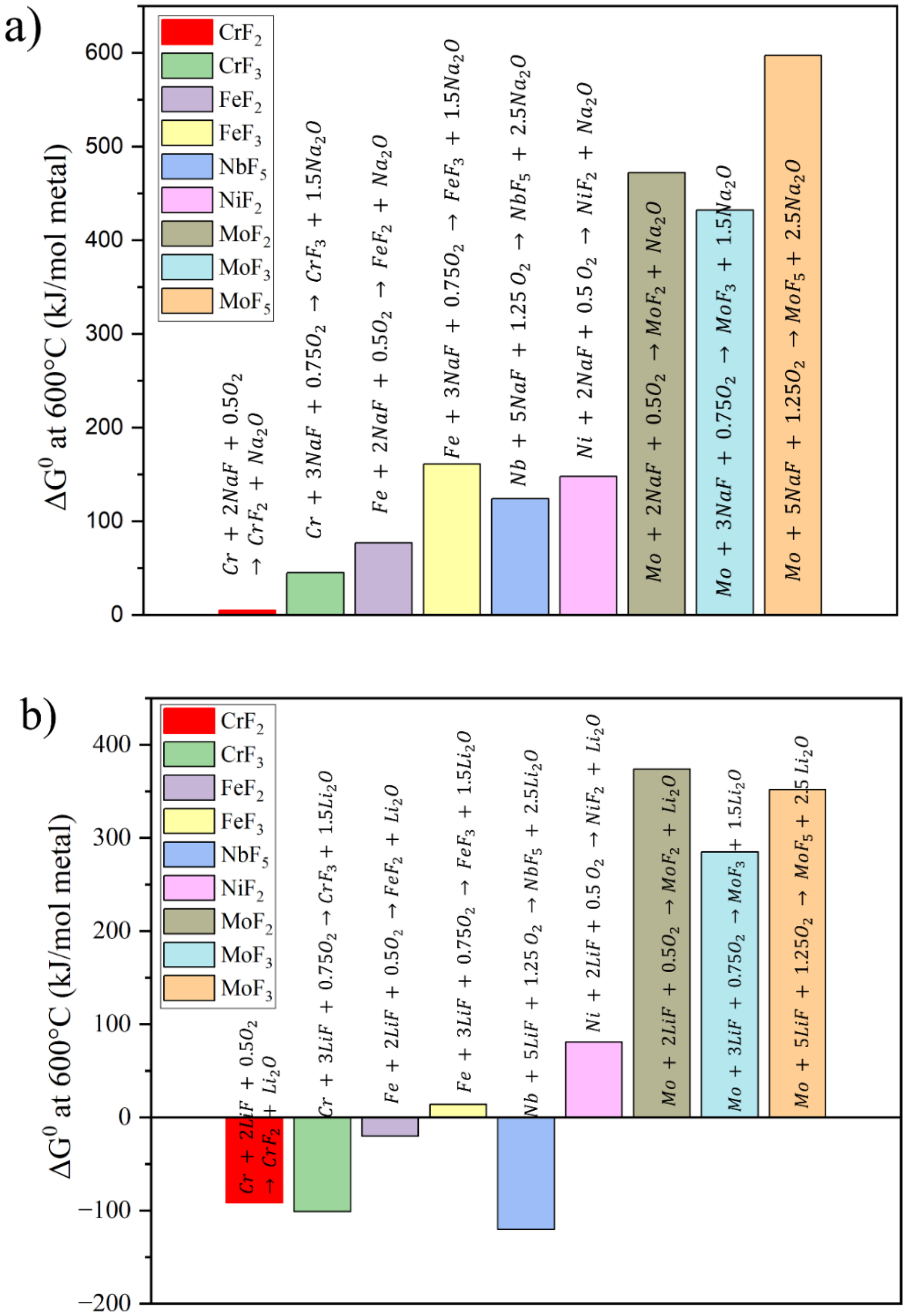

Figure 26) Gibbs free reaction energies for different metals in contact to a) NaF b) LiF at 600°C.

The formation and stability of metal fluorides was investigated over a temperature range of 50-600°C and presented in figure 27. Reaction 26 was used in this case as well and calculations were kept consistent based on per metal atom. The stabilities do not show a significant difference compared to the plotted values for 600°C illustrated in figure 26b. However, there was a difference in the spontaneous formation of FeF_3 which is unstable at temperatures higher than 500°C and forms at lower temperatures.

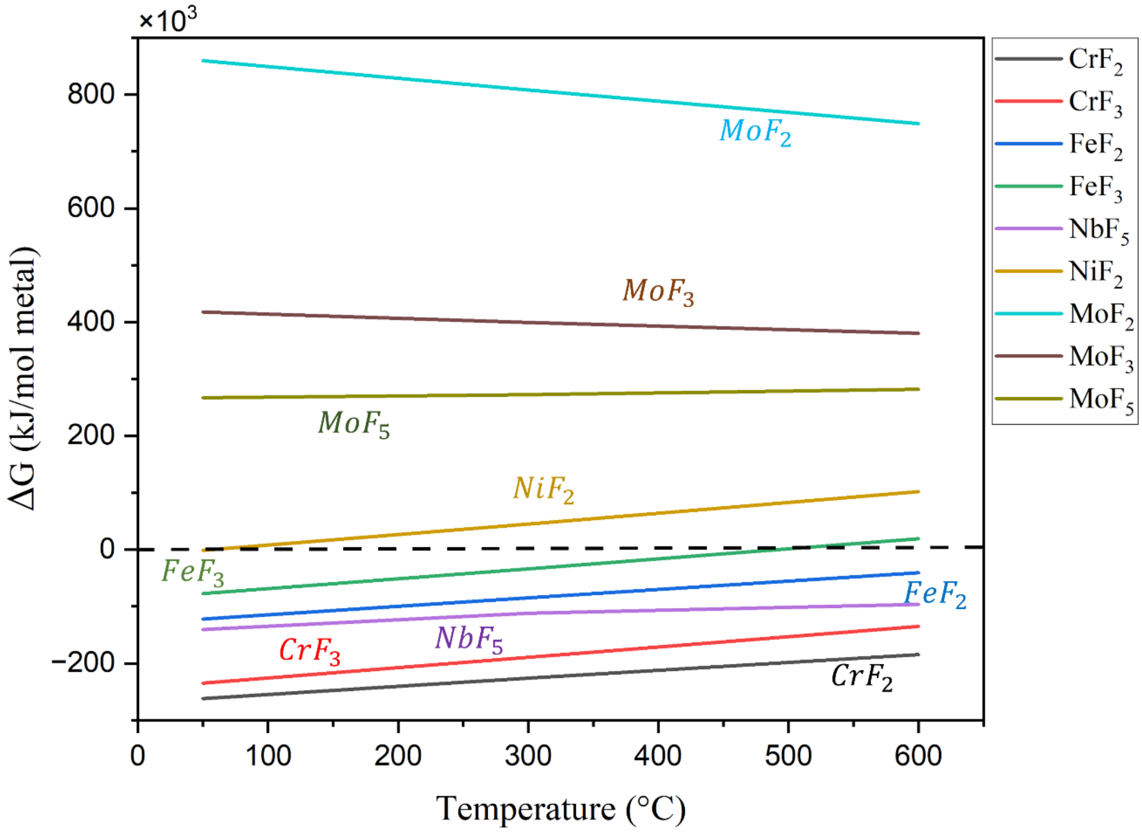

Figure 27) Gibbs free reaction energies for different metals in contact with LiF over a range of temperature from 50-600°C.

5.Discussion

5.1 Corrosion Mechanism in LiF

The extent of the internal attack was different in the three different scenarios discussed, however, the corrosion mechanism which applies is the same. The LiF corrosion mechanism will be discussed in detail during 168 and 1000 hours of exposures.

Reaction 26 is the underlying redox-reaction between metal, salt and oxygen. The energetically driving net reaction is oxidation of metal atoms by oxygen. As can be seen in reaction 26, the alkali metal (A= Li in this case) and fluoride ions hold to their oxidation states during the corrosion process, although they may separate to form other stable compounds (metal fluorides and lithium oxide). The oxidation of the metal (inner anode) takes place through oxygen reduction (outer cathode), while reduced oxygen and metal cations in the alloy may not come into immediate contact. According to reaction 26, in case the alkali oxide (A_2O in this case = lithium oxide) is stable, oxygen ions get charge compensated by the alkali cation while fluoride would be free to diffuse into the metal grain boundaries. Fluoride needs to find the equivalent charge compensation at the cation evolution site which is located at the inner anode. It is worth mentioning that lithium has maintained its oxidation state before and after forming the lithium oxide and reduction of the outer cathode (oxygen) has taken place by the oxidation of the inner anode.

As long as the alkali oxide (A_2O) is stable, and at least one of the alloying elements forms a stable metal fluoride, reaction 26 would be spontaneous. As shown in table 2, in LiF exposures, reaction 26 is energetically spontaneous for some of the transition metal fluorides (FeF_2, CrF_2, CrF_3 and NbF_5). This is in line with the EDS results where Cr, Fe and Nb depletion was seen underneath the oxide scale. Since both components in the lithium fluoride salt (Li and F) form stable compounds in these cases, the inner anode, outer cathode mechanism is valid, and fluoride would leave its alkali partner to diffuse into the metal. This is while trivalent iron fluoride as well as molybdenum and nickel fluorides show $\Delta G>0$ and thus do not form spontaneously.

Figure 28 illustrates this mechanism showing that fluoride ion is in its anionic state during the whole mechanism. As shown in figure 28, when fluoride enters the grain boundaries of the metal, it will not leave the metal/oxide interface again to diffuse into the oxide but will diffuse deeper as more fluoride ions continue to enter the grain boundaries of the metal. In short exposures, when the metal grain boundaries are not depleted and diffusion of the alloying elements takes relatively short time, fluoride anions are charge compensated by metal cations. The metal cations are accessible enough in this case, to fill the cationic positions in the metal and charge compensate for fluoride.

The diffusion of fluoride into the metal grain boundaries and the formation of transition metal fluorides would accelerate the transport of metal cations to the metal/oxide interface. However, once alloying elements reach the metal/oxide interface where lithium oxide exists, they tend to form alkali metal oxides. This is where fluoride anion will not charge compensate for the metal cations and fluoride anion is free to diffuse deeper. TOF-SIMS results after 168 hours of exposure in LiF, showed no lithium-ion diffusion in the upper grain boundaries underneath the metal/oxide interface. Unlike lithium, fluoride ion presence was confirmed in the upper grain boundaries. This contrast confirmed that lithium and fluoride do not diffuse together as an ionic compound. This was in line with reaction 26 and separation of the ionic partners in LiF in case of the spontaneity of the formation of metal fluorides.

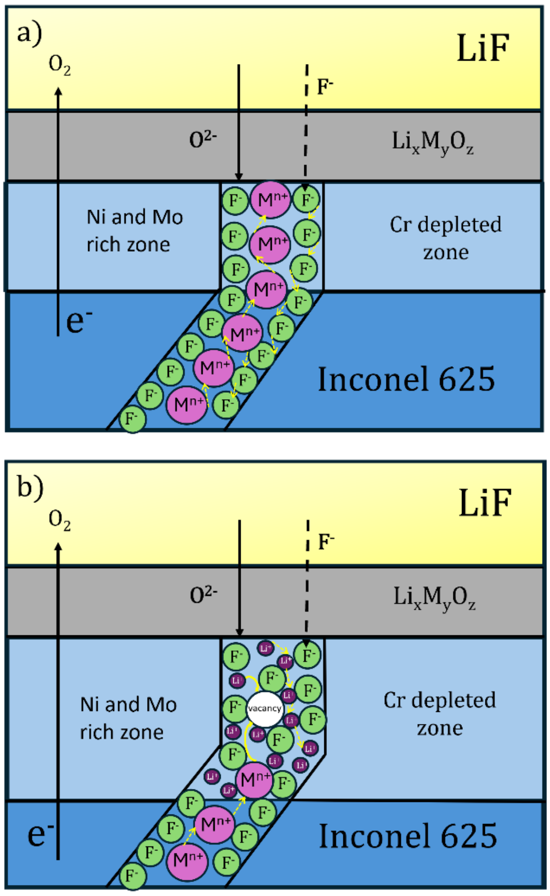

Figure 28) Suggested diffusion paths for a) short LiF exposures b) long LiF exposures.

The absence of lithium in grain boundaries after short exposures clarified that lithium and fluoride do not diffuse into the metal grain boundaries together. After long exposures, however, lithium diffusion was seen in the upper and wider grain boundaries. Figure 28b illustrates the suggested mechanism in case of longer exposures, where the depletion zone comprising mainly of nickel and molybdenum (which have not formed their corresponding metal fluorides) is thicker. After long exposures, less noble elements in the upper metal grain boundaries have already been transported to the oxide scale. Hence, the upper grain boundaries are wide open and exhausted from losing the less noble alloying elements. In this case, when more fluoride has also diffused into the grain boundaries, metal cations need to diffuse from grain boundaries located deeper in the metal, to the depletion zone to charge compensate for the fluoride ions. Considering that this diffusion can take long, lithium ions from the LiF deposit can scramble into the wide open, upper grain boundaries to make this charge compensation happen. As shown in figure 28b, the cationic position created by fluoride diffusion in the metal can be taken by either the alloying elements or lithium. In long exposures lithium has an easier time than the alloy metals to diffuse in and take that vacancy to charge compensate for the anionic species.

SEM and EDS results showed that Inconel 625 responded differently to the two different salts of LiF and NaF which it was exposed to in an oxidizing environment. The stability of transition metal fluorides in contact with LiF and NaF was presented in figure 26. The calculations behind for LiF and NaF exposures can be found in table 2 and 3 respectively.

Table 2) Gibbs enthalpies retrieved from Factsage 7.3 [59] for relevant reactions for transition metal fluorides in LiF/O2 environment

No	$reaction$	$Reaction\ \Delta G\ ^{0}_{600°C}$ $\frac{kJ}{mol\ metal}$	compound
	$Reactions\ at\ an\ inner\ anode\ and\ outer\ cathode$		
R 27	$Cr + 2LiF + 0.5O_2 \rightarrow CrF_2 + Li_2O$	-92	CrF_2
R 28	$Cr + 3LiF + 0.75O_2 \rightarrow CrF_3 + 1.5Li_2O$	-101	CrF_3
R 29	$Fe + 2LiF + 0.5O_2 \rightarrow FeF_2 + Li_2O$	-20	FeF_2
R 30	$Fe + 3LiF + 0.75O_2 \rightarrow FeF_3 + 1.5Li_2O$	$+14$	FeF_3
R 31	$Nb + 5LiF + 1.25\ O_2 \rightarrow NbF_5 + 2.5Li_2O$	-120	NbF_5
R 32	$Ni + 2LiF + 0.5\ O_2 \rightarrow NiF_2 + Li_2O$	$+81$	NiF_2
R 33	$Mo + 2LiF + 0.5O_2 \rightarrow MoF_2 + Li_2O$	$+374$	MoF_2
R 34	$Mo + 3LiF + 0.75O_2 \rightarrow MoF_3 + 1.5Li_2O$	$+285$	MoF_3
R 35	$Mo + 5LiF + 1.25O_2 \rightarrow MoF_5 + 2.5Li_2O$	$+352$	MoF_5

Reactions in table 2 are written based on reaction 26 where we have suggested how metal fluorides form in relation to the alkali oxide. This reaction explains how fluoride is driven into the metal via the coupling between the inner anode and the outer cathode. Based on this reaction, the fluoride release into the metal and formation of metal fluorides is bound to the stability of the alkali oxide species (in this case Na_2O or Li_2O). Considering the fact that LiF and NaF are very stable, dissociation of the cationic and anionic parts happens only if both of them get involved in stable compounds of transition metal fluorides (MF_n) and alkali oxide (A_2O).

In this reaction, fluoride ion (F^-) and lithium cation (Li^+) never change oxidation states and will always remain in their ionic forms. Considering the fact that the corresponding alkali oxide varies based on the alkali fluoride used, the stability of the transition metal fluorides in contact with different salts (alkali fluorides) can vary, although the metal fluorides are the same. Hence, the stability of the transition metal fluorides has to be calculated separately for each alkali halogenide and cannot be applied from one environment to another.

In contrast to fluoride which maintains its (-1) oxidation state, oxygen is getting reduced in reaction 26 and the transition metal (M) is getting oxidized. In case reaction 26 is spontaneous, the metal component which is getting oxidized forms the inner anode and oxygen which is getting reduced forms the outer cathode.

Role of Thermal Gradient and Extended Cathode

In Scenario 1, the coupon sample exposed to 600 °C was part of a metallic strip subjected to a temperature gradient. Sections of the strip exposed to lower temperatures remain electrically connected to regions experiencing higher temperatures. Due to the design of the setup and the use of long alumina crucibles housing the samples, the air inlet is positioned at the top of the crucibles (Figure 9a, b). Consequently, the upper regions of the strip (exposed to relatively lower temperatures) have greater access to oxygen. The electrical conductivity along the entire metal strip enables the cathodic oxygen reduction reaction to occur throughout, particularly in the upper sections where the oxygen partial pressure is presumed higher. Nonetheless, since the strip maintains electrical conductivity, atoms from the region exposed to the highest temperatures can diffuse more rapidly to the metal/oxide interface and become oxidized. This would mean that oxidation and reduction do not necessarily have to happen at the same site.

Consequently, oxygen reduction is not confined to the hottest section but may occur at various points along the strip. As shown in figure 29, the extended surface area of the strip facilitates greater oxygen reduction, which correspondingly leads to increased oxidation of metal atoms. As oxygen reduction takes place both at the high-temperature region and elsewhere on the strip, a larger proportion of electrons from the metal is consumed in the reduction process.

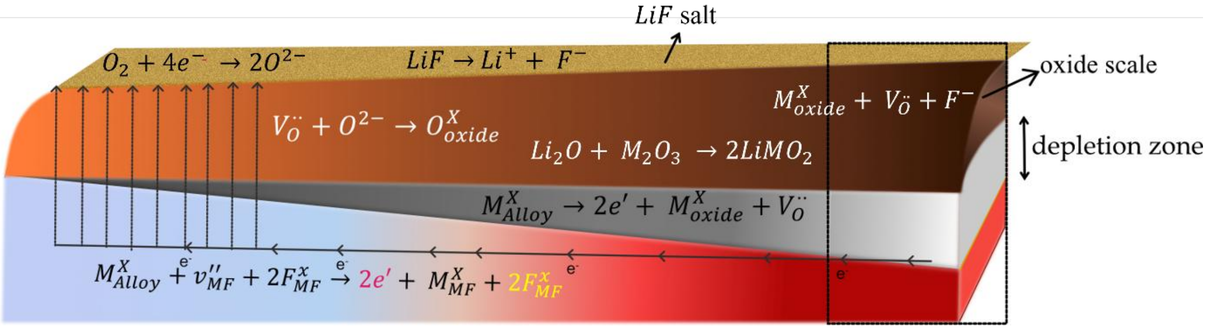

Figure 29) Overview of the thermal gradient strip, where anodic reaction is faster at the hottest section.

Metal atom diffusion occurs at an increased rate in regions subjected to higher temperatures, resulting in a potentially greater availability of cations at the metal/oxide interface in the lower sections of the strip. Consequently, although oxidation of metal atoms occurs across the entire strip, the hottest section (where diffusion is more rapid) is likely to be more significantly impacted by fluoride attack. This implies that oxidation of the inner anode, located in the high-temperature region, is intensified under these conditions. This observation may account for the more pronounced intergranular attack observed in the coupon exposed to a temperature gradient, relative to the single coupon positioned beneath a static column of salt. In order to distinguish between the vacancies in the metal and oxide, the positions have been mentioned as subscripts in figure 29. A neutral metal position in the alloy is denoted as M^x_{Alloy} while a positively charged (oxygen) vacancy is denoted as $V_{\ddot{O}}$.

Initially, the metal, which is electrically neutral in the alloy phase at the metal-oxide interface, undergoes polarization by mobilizing electrons to a cathode elsewhere. This results in the formation of a metal cation within the oxide lattice, represented as M^x_{oxide} , indicating that the cation occupies a lattice site without deviation from its formal charge state. The formation of an oxygen vacancy $V_{\ddot{O}}$ occurs in the same lattice, representing a doubly positively charged anionic vacancy. This vacancy can be subsequently occupied either by a fluoride or by oxygen anion. When filled by an oxygen anion (O^{2-}), the combined defect complex remains electrically neutral, while incorporation of a fluoride ion (F^-) only partially compensates the charge. It thereby injects a defect in an oxide lattice, resulting in a singly positively charged state due to the monovalent nature of fluoride.

Fluoride retains its negative charge throughout the process and is denoted as $F_{MF_n}^x$ to reflect its intrinsic charge neutrality within its site. Metal cations populate the cationic vacancies associated with fluoride migration which are generated upon electron consumption at a cathode elsewhere. Metal cations, initially present in the metallic state with an oxidation state of zero, transition to higher oxidation states upon the formation of metal fluorides (e.g.,MF_2) but remain charge-balanced within their lattice positions (M_{MF}^x). The entry of fluoride ions into the metallic grain boundary generates a negatively charged metal vacancy (V_{MF}'), which must be compensated by metal cations to maintain local charge balance. This enables fluoride incorporation through a mechanism reliant on the availability of cationic vacancies, without which fluoride incorporation into the metallic phase is thermodynamically unfavorable.

Scenario 2 involves oxygen permeation through a salt column above the coupon, located at the base of the alumina crucible. The confinement of oxygen reduction to the limited surface area of the coupon explains the diminished extent of corrosion in this case. Furthermore, the necessity for oxygen to permeate through a 50 cm column of salt to reach the coupon implies a lower oxygen partial pressure at the bottom compared to the upper zones of the long crucible.

Previous studies have shown that weight gain in nickel samples rises with increasing salt application, reaching a peak at approximately 0.30 mg/cm² [60]. Beyond this point, only negligible further gains were observed, reportedly due to a plateau in oxygen uptake despite continued increases in the concentration of oxyanion-containing salts up to 1.2 mg/cm² [60]. This limitation was ascribed either to the exhaustion of available metal or to the restricted ability of molten carbonate to facilitate further oxygen incorporation. In the current study, salt coverage was significantly increased. Results from scenarios 2 and 3 in LiF extend the prior observations, indicating that further addition of deposit may actually suppress oxygen uptake due to physical kinetic barriers impeding oxygen access at the metal/oxide interface. The extended outer cathode was absent in both of scenarios 2 and 3; however the extent of oxygen reduction could be different, due to different oxygen partial pressures on the surface of the coupons.

The absence of an extended outer cathode in Scenario 2 results in reduced corrosion and shallower fluoride ingress through intergranular attack. The lower rate of oxygen reduction corresponds to decreased oxidation on the metal side. Consequently, the reduced polarization of the alloy accounts for the limited fluoride penetration and less severe intergranular degradation.

In comparison with the gradient study, the depth of the intergranular attack was less in scenario 2. The content of Cr, Fe and Nb in alloy 625 are way less than Ni, this would mean that the intergranular attack facilitates the transport of these alloying elements from the inner anode to the outer cathode. Hence, a shallower intergranular attack in scenario 2, would translate to a smaller share of these alloying elements in the oxide scale.

A thicker and uneven oxide scale was observed in scenario 3, which indicated a higher amount of oxygen reduction on the sample surface. The higher rate of oxygen reduction led to more polarization and oxidation in the alloy which would translate to more fluoride ingress, since fluoride can get charge compensated by the polarized metal. This can justify the thicker and harsher fluoride attack into the metal which led to higher fluoride uptake by the metal.

5.2 Corrosion Mechanism in NaF

As discussed in the context of LiF exposures, the stability of transition metal fluorides is influenced by the specific alkali fluoride present and cannot be generalized across different environments. The instability of all metal fluorides in contact with NaF is demonstrated in figure 26a, and the thermodynamic calculations underlying this figure are addressed in table 3. The spontaneity of reaction 26 was evaluated for various alloying elements in the alloy in contact with NaF. This reasoning also applies to NaF environments, where the formation of a stable metal fluoride would be a prerequisite for electrochemical coupling between the inner anode and the outer cathode. In this context, the stability of metal fluorides depends on the presence of sodium oxide. Table 3 presents the results of these stability assessments, showing that none of the metal fluorides are stable in contact with NaF. This suggests that the alkali metal does not form a stable oxide in the presence of NaF, thereby preventing the dissociation of the alkali metal and its fluoride anion. Consequently, as the release of fluoride is bound to the stability of alkali oxide species, fluoride ions are also unlikely to diffuse into the metal grain boundaries.

Table 3) Gibbs enthalpies retrieved from Factsage 7.3 [59] for relevant reactions for metal fluorides in NaF/O2 environment

No	$reaction$	$Reaction\ \Delta G\ ^{0}_{600°C}\ \frac{kJ}{mol}$	compound
	$Reactions\ at\ an\ inner\ anode\ and\ outer\ cathode$		
R 36	$Cr + 2NaF + 0.5O_2 \rightarrow CrF_2 + Na_2O$	+5	CrF_2
R 37	$Cr + 3NaF + 0.75O_2 \rightarrow CrF_3 + 1.5Na_2O$	+45	CrF_3
R 38	$Fe + 2NaF + 0.5O_2 \rightarrow FeF_2 + Na_2O$	+77	FeF_2
R 39	$Fe + 3NaF + 0.75O_2 \rightarrow FeF_3 + 1.5Na_2O$	+161	FeF_3
R 40	$Nb + 5NaF + 1.25\,O_2 \rightarrow NbF_5 + 2.5Na_2O$	+124	NbF_5
R 41	$Ni + 2NaF + 0.5\,O_2 \rightarrow NiF_2 + Na_2O$	+149	NiF_2
R 42	$Mo + 2NaF + 0.5O_2 \rightarrow MoF_2 + Na_2O$	+472	MoF_2
R 43	$Mo + 3NaF + 0.75O_2 \rightarrow MoF_3 + 1.5Na_2O$	+432	MoF_3
R 44	$Mo + 5NaF + 1.25O_2 \rightarrow MoF_5 + 2.5Na_2O$	+597	MoF_5

The inner anode outer cathode mechanism did not apply in NaF case, hence the suggested mechanism will be modified. Figure 30 illustrates the NaF-driven corrosion in which metal atoms get oxidized and oxygen gets reduced in return. The oxidation of the metal and the reduction of oxygen atoms in this mechanism take place through the formation of an electrolyte. This fluxing electrolyte consists of metal cations together with oxygen and sodium fluoride at the metal/oxide interface. Alkali halogenide ions remain charge compensated in the flux media but do not participate in stable new compounds. This fluxing electrolyte transports metal cations to oxygen and leads to the formation of a porous oxide on top. Since the alkali oxide (sodium oxide) was not stable in this case, the alkali fluoride species separated from the transition metal oxide. As none of the reactions in table 3 were spontaneous, none of the metal fluorides in this case were stable. This is in line with the absence of both depletion zone and intergranular attack in NaF exposures. Hence, sodium was never part of the metal oxide and the oxide layer consisted of islands of sodium fluoride and metal oxide separate from each other.

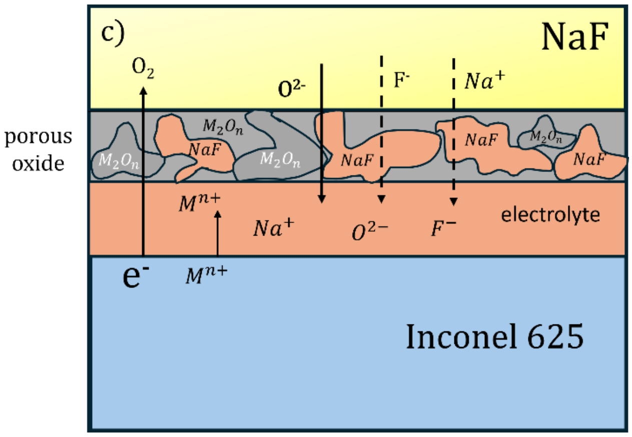

Figure 30. Suggested corrosion mechanism for NaF exposures.

5.3 Thermodynamic Feasibility of Fluorine Gas Formation

As previously mentioned in the literature review part, thermodynamic calculations for the formation of metal fluorides was previously based on fluorine gas in literature [8]. While these calculations clarified the tendency or affinity of different alloying elements to be attacked in molten fluorides [28], they are not system specific. One could not conclude if/which metal fluorides exist in a specific alkali fluoride system and oxidizing condition including impurity level. With this being said, several corrosion studies base the cause of the attack on spontaneous release of fluorine from the environment [11]. However, in the current study the presence of fluorine gas in contact with alkali fluoride salts where fluorine is not actively injected into the system is rejected.

In our mechanism, fluoride and lithium never change oxidation state and are always in their ionic forms. There are other oxidizing elements in our mechanism which drive the oxidation of the metal. In our oxidizing environment, oxygen oxidizes the metal, which can be at an impurity level in non-oxidizing environments. The amount of oxygen is less in those environments, so is the intensity of corrosion. In addition, having humidity and HF as an impurity can also drive the oxidation of the metal.

One of the misinterpretations for the source of fluorine gas is a mechanism entitled "active oxidation", which was previously discussed in the literature review section. Considering the need for the formation of F_2 in this mechanism, we want to thermodynamically calculate if it is possible to generate fluorine gas in contact with NaF or LiF. There are two main routes through which fluorine gas is discussed to be generated in the theory of active oxidation. The spontaneity of these reactions is investigated in the following section.

1) The oxidation of HF as a gas and formation of fluorine gas molecules and water:

$$2HF\ (g) + \ ½\ O_2\ (g) \rightarrow\ F_2\ (g) + \ H_2O\ (g) \qquad R\ 45$$

$$\Delta G\ ^{0}_{50°C} = \ +316kJ \qquad \Delta G\ ^{0}_{800°C} = \ +368kJ$$

The energetic values for the oxidation of HF at a temperature range of 50-800°C shows that the generation of fluorine gas is not energetically favored.

2) The reaction of condensed alkali fluorides with oxygen with or without the participation of different oxide scales would also be considered as a source of fluorine gas generation, if active oxidation was to apply. Considering A as the alkali metal and M as iron or chromium would lead to the following reactions in this case:

$$2AF + M_2O_3 + \ ½\ O_2 \rightarrow\ 2AMO_2 + F_2 \qquad (A = Li, Na), M = transition\ metal \qquad R\ 46$$

$$4AF + M_2O_3 + \ ^{5}/_{2}\ O_2 \rightarrow\ 2A_2MO_4 + 2F_2 \qquad (A = Li, Na), M = transition\ metal \qquad R47$$

$$2AF + \frac{1}{2}\ O_2\ \rightarrow A_2O + F_2 \qquad (A = Li, Na)$$

R 48

Table 4) Gibbs enthalpies for reactions proposed for the so-called "active oxidation" theory, showing thermodynamic non-spontaneity

No	$reaction$	$Reaction\ DG\ ^{0}_{800°C}$ $in\ kJ$	$Reaction\ DG\ ^{0}_{50°C}$ $in\ kJ$
R 49	$2NaF + \ Cr_2O_3 + 0.5O_2\ \rightarrow 2NaCrO_2 + \ F_2$	+572	+618
R 50	$2NaF + \ Fe_2O_3 + 0.5O_2\ \rightarrow 2NaFeO_2 + \ F_2$	+509	+551
R 51	$2LiF + \ Fe_2O_3 + 0.5O_2\ \rightarrow 2LiFeO_2 + \ F_2$	+459	+521
R 52	$4NaF + \ Cr_2O_3 + 2.5O_2\ \rightarrow 2Na_2CrO_4 + \ 2F_2$	+774	+758
R 53	$4LiF + \ Cr_2O_3 + 2.5O_2\ \rightarrow 2Li_2CrO_4 + \ 2F_2$	+805	+815
R 54	$2LiF + \frac{1}{2}\ O_2\ \rightarrow Li_2O + F_2$	+618	+975
R 55	$2NaF + \frac{1}{2}\ O_2\ \rightarrow Na_2O + F_2$	+709	+657

The energetic values for not all the oxides were available in Factsage 7.3, hence calculations are limited to the oxides with available energetic values. None of the reactions considered in part 1 (oxidation of HF) and part 2 were spontaneous. This would mean that fluorine gas would not spontaneously been generated in LiF corrosion in oxidizing conditions and the theory of active oxidation does not apply in this case. The Gibbs free energy was calculated over a temperature range of 50-800 °C and none of the reactions were still spontaneous.

In all of these reactions fluoride is getting oxidized changing oxidation state from -1 to 0, while oxygen is being reduced, changing oxidation state from 0 to -2. Fluorine is the most electronegative element and the strongest oxidizer which combines with most of the organic and inorganic materials. Hence, oxidizing fluoride does not happen spontaneously in any of the tested reactions and temperatures.

6.Summary

By coupling thermodynamic calculations with isothermal/thermal-gradient exposures followed by multi-technique characterization including SEM/EDS, XRD, and TOF-SIMS, this thesis clarifies corrosion mechanisms for Inconel 625 in alkali fluorides.

Paper I: *High temperature corrosion in LiF salt containing oxygen*

1) Exposing a sample as a part of a metal strip showed that having a temperature gradient over an extended cathode area accelerates the breakdown of the alloy in comparison with a similar isothermal exposure.
2) The extent of corrosion strongly depends on the amount of oxygen that can reach the metal surface in both isothermal and thermal gradient experiments. Higher oxygen access promotes deeper fluoride penetration and higher corrosion rates.

Paper П: *Redox Mechanisms and Metal Fluoride Stability in Alkali Fluoride Corrosion*

1) Previous literature has thermodynamically investigated metal fluoride formation by considering the reaction of metals with fluorine gas. However, in this study, we propose an alternative for calculating Gibbs free energies for the underlying corrosion reactions. In the suggested approach, the cathodic oxygen reduction reaction and the anodic oxidation of the metal components are not necessarily at the same location.
2) Thermodynamic calculations for the formation of metal fluorides in the presence of NaF and air, showed positive Gibbs free reaction energies for all alloying elements, consistent with the experimental observations. In contrast, calculations for LiF revealed negative Gibbs free reaction energy values for the formation of CrF_2, CrF_3, FeF_2, and NbF_5, which aligns with the intergranular depletion of Cr, Nb, and Fe.
3) Basing our studies on an outer cathode inner anode redox mechanism, the corrosion mechanism driven by LiF was distinguished from NaF. This study demonstrates intergranular attack for the corrosion attack in the presence of LiF, while no such attack was detected in contact with NaF.

7.Outlook

As discussed in the results section, the formation of low-melting-point compounds is expected under both LiF and NaF exposures. In particular, the formation of such compounds in NaF environments likely explains the high corrosion rate and oxide spallation observed. Therefore, it is essential to calculate the eutectic compositions that may form at various temperatures between metal fluorides and oxides, as well as between alkali fluorides and transition metal fluorides.

Furthermore, the thermal gradient exposures (of which only the 600 °C coupon was previously discussed) should be examined more comprehensively. Investigating the metal behavior across different temperatures would reveal how colder sections act as extended cathodes, allowing a comparison of corrosion severity with single isothermal exposures. Additionally, the behavior of various alloying elements and the potential formation of transition metal fluorides have been evaluated. Alloys containing more corrosion-resistant elements could be tested and utilized as either coatings or bulk materials to mitigate corrosion. The role of intermetallic phases is also relevant; assessing whether these microstructural intermetallics inhibit or accelerate corrosion is of particular interest.

8.Bibliography

1. Xu, J., et al., *A review of processes and technologies for the recycling of lithium-ion secondary batteries.* Journal of Power Sources, 2008. **177**(2): p. 512-527.
2. European Commission, E., *Waste statistics - recycling of batteries and accumulators*.
3. Emilsson, E. and L. Dahllöf, *Lithium-ion vehicle battery production-status 2019 on energy use, CO2 emissions, use of metals, products environmental footprint, and recycling*. 2019, IVL Svenska Miljöinstitutet.
4. Etude, M.C., et al., *Recycling lithium-ion batteries: a review of current status and future directions.* Sustainable Chemistry One World, 2024: p. 100027.
5. Latini, D., et al., *A comprehensive review and classification of unit operations with assessment of outputs quality in lithium-ion battery recycling.* Journal of Power Sources, 2022. **546**: p. 231979.
6. Sobianowska-Turek, A., et al., *The necessity of recycling of waste li-ion batteries used in electric vehicles as objects posing a threat to human health and the environment.* Recycling, 2021. **6**(2): p. 35.
7. Neumann, J., et al., *Recycling of lithium-ion batteries—current state of the art, circular economy, and next generation recycling.* Advanced energy materials, 2022. **12**(17): p. 2102917.
8. Olson, L.C., et al., *Materials corrosion in molten LiF–NaF–KF salt.* Journal of Fluorine Chemistry, 2009. **130**(1): p. 67-73.
9. Wang, Y., C. Zeng, and W. Li, *The influence of temperature gradient on the corrosion of materials in molten fluorides.* Corrosion Science, 2018. **136**: p. 180-187.
10. Misra, A.K. and J.D. Whittenberger. *Fluoride salts and container materials for thermal energy storage applications in the temperature range 973–1400 K*. in *22nd Intersociety Energy Conversion Engineering Conference*. 1987. American Institute of Aeronautics and Astronautics.
11. Wang, Y., et al., *Material corrosion in molten fluoride salts.* International Journal of Electrochemical Science, 2018. **13**(5): p. 4891-4900.
12. Sohal, M.S., et al., *Engineering database of liquid salt thermophysical and thermochemical properties*. 2010, Idaho National Lab.(INL), Idaho Falls, ID (United States).
13. Eriksson, J.-E., et al., *The effect of Cl, Br, and F on high-temperature corrosion of heat-transfer alloys.* Fuel, 2023. **348**: p. 128516.
14. Thompson, D.L., et al., *The importance of design in lithium ion battery recycling–a critical review.* Green Chemistry, 2020. **22**(22): p. 7585-7603.
15. Nitta, N., et al., *Li-ion battery materials: present and future.* Materials today, 2015. **18**(5): p. 252-264.
16. Li, M., et al., *New concepts in electrolytes.* Chemical reviews, 2020. **120**(14): p. 6783-6819.
17. Xu, K., *Nonaqueous liquid electrolytes for lithium-based rechargeable batteries.* Chemical reviews, 2004. **104**(10): p. 4303-4418.
18. Choi, J. and P.J. Kim, *A roadmap of battery separator development: Past and future.* Current Opinion in Electrochemistry, 2022. **31**: p. 100858.
19. Zheng, X., et al., *A mini-review on metal recycling from spent lithium ion batteries.* Engineering, 2018. **4**(3): p. 361-370.

20. Lebedeva, N.P. and L. Boon-Brett, *Considerations on the chemical toxicity of contemporary Li-ion battery electrolytes and their components.* Journal of The Electrochemical Society, 2016. **163**(6): p. A821.
21. Tanong, K., J.-F. Blais, and G. Mercier, *Metal recycling technologies for battery waste.* Recent Patents on Engineering, 2014. **8**(1): p. 13-23.
22. Kwade, A. and J. Diekmann, *Recycling of lithium-ion batteries.* The LithoRec Way, Sustainable Production, Life Cycle Engineering and Management, 2018. **53**.
23. Velázquez-Martínez, O., et al., *A critical review of lithium-ion battery recycling processes from a circular economy perspective.* Batteries, 2019. **5**(4): p. 68.
24. Murakami, Y., et al., *Erosion mechanism of refractories in a pyro-processing furnace for recycling lithium-ion secondary batteries.* Ceramics International, 2020. **46**(7): p. 9281-9288.
25. Ren, G.-x., et al., *Recovery of valuable metals from spent lithium ion batteries by smelting reduction process based on FeO–SiO2–Al2O3 slag system.* Transactions of Nonferrous Metals Society of China, 2017. **27**(2): p. 450-456.
26. Sonoc, A., J. Jeswiet, and V.K. Soo, *Opportunities to improve recycling of automotive lithium ion batteries.* Procedia cIRP, 2015. **29**: p. 752-757.
27. Ozeryanaya, I., *Corrosion of metals by molten salts in heat-treatment processes.* Met. Sci. Heat Treat. Met.(Engl. Transl.);(United States), 1985. **27**(3).
28. Sridharan, K. and T. Allen, *Corrosion in molten salts*, in *Molten salts chemistry*. 2013, Elsevier. p. 241-267.
29. Mansfeld, F., N. Paton, and W. Robertson, *The high temperature behavior of superalloys exposed to sodium chloride: II. corrosion.* Metallurgical Transactions, 1973. **4**: p. 321-327.
30. Kondo, M., et al., *Corrosion characteristics of reduced activation ferritic steel, JLF-1 (8.92 Cr–2W) in molten salts Flibe and Flinak.* Fusion Engineering and Design, 2009. **84**(7-11): p. 1081-1085.
31. DeVan, J.H., *Effect of alloying additions on corrosion behavior of nickel-molybdenum alloys in fused fluoride mixtures.* 1960.
32. Olson, L.C., et al., *Impact of corrosion test container material in molten fluorides.* Journal of Solar Energy Engineering, 2015. **137**(6): p. 061007.
33. Banerjee, R.H., et al., *Investigating Cr dealloying and Li ingress in Ni-Mo-Cr alloys with different Mo/Cr ratio exposed to FLiNaK salt.* Corrosion Science, 2023. **212**: p. 110929.
34. Williams, D., *Assessment of candidate molten salt coolants for the NGNP/NHI heat-transfer loop*. 2006, Oak Ridge National Lab.(ORNL), Oak Ridge, TN (United States).
35. Ren, W., et al. *Considerations of alloy N for fluoride salt-cooled high-temperature reactor applications*. in *Pressure Vessels and Piping Conference*. 2011.
36. Ye, X.-X., et al., *The high-temperature corrosion of Hastelloy N alloy (UNS N10003) in molten fluoride salts analysed by STXM, XAS, XRD, SEM, EPMA, TEM/EDS.* Corrosion Science, 2016. **106**: p. 249-259.
37. Olander, D., *Redox condition in molten fluoride salts: Definition and control.* Journal of Nuclear Materials, 2002. **300**(2-3): p. 270-272.
38. Johnson, G.K., *The enthalpy of formation of FeF3 by fluorine bomb calorimetry.* The Journal of Chemical Thermodynamics, 1981. **13**(5): p. 465-469.
39. Zhou, H., et al., *Controlled formation of mixed nanoscale domains of high capacity Fe2O3–FeF3 conversion compounds by direct fluorination.* ACS nano, 2015. **9**(3): p. 2530-2539.

40. Liu, T., et al., *Corrosion of alloys in high temperature molten-salt heat transfer fluids with air as the cover gas.* Solar Energy, 2019. **191**: p. 435-448.
41. Wang, Y.L., et al., *Effects of the oxidants H2O and CrF3 on the corrosion of pure metals in molten (Li, Na, K) F.* Corrosion Science, 2016. **103**: p. 268-282.
42. Wu, H., P. Yrjas, and M. Hupa, *Laboratory studies of potassium-halide-induced high-temperature corrosion of superheater steels. Part 1: exposures in dry air.* Energy & Fuels, 2015. **29**(2): p. 1186-1195.
43. Grabke, H., E. Reese, and M. Spiegel, *The effects of chlorides, hydrogen chloride, and sulfur dioxide in the oxidation of steels below deposits.* Corrosion science, 1995. **37**(7): p. 1023-1043.
44. Asteman, H. and M. Spiegel, *Investigation of the HCl (g) attack on pre-oxidized pure Fe, Cr, Ni and commercial 304 steel at 400 C.* Corrosion Science, 2007. **49**(9): p. 3626-3637.
45. Enestam, S., et al., *Are NaCl and KCl equally corrosive on superheater materials of steam boilers?* Fuel, 2013. **104**: p. 294-306.
46. Folkeson, N., L.-G. Johansson, and J.-E. Svensson, *Initial stages of the HCl-induced high-temperature corrosion of alloy 310.* journal of the electrochemical society, 2007. **154**(9): p. C515.
47. Lindmark, H., T. Jonsson, and J. Liske, *A time-resolved study of PbCl2-induced corrosion of low-alloyed steel in the presence of water vapour at 400° C.* Corrosion Science, 2024. **229**: p. 111843.
48. Kofstad, P., *High Temperature Corrosion*. 1988: Elsevier Applied Science.
49. Crankovic, G.M., *ASM Handbook, Volume 10:.: Materials Characterization*. 1986: ASM International.
50. Zhou, W., et al., *Fundamentals of scanning electron microscopy (SEM).* Scanning microscopy for nanotechnology: techniques and applications, 2007: p. 1-40.
51. Österreicher, J.A., et al., *Spatial lithium quantification by backscattered electron microscopy coupled with energy-dispersive X-ray spectroscopy.* Scripta Materialia, 2021. **194**: p. 113664.
52. Pantano, C.G., *Secondary ion mass spectroscopy.* 1986.
53. Sodhi, R.N., *Time-of-flight secondary ion mass spectrometry (TOF-SIMS):—versatility in chemical and imaging surface analysis.* Analyst, 2004. **129**(6): p. 483-487.
54. Panda, B., *Secondary Ion Mass Spectroscopy.* ASM Handbook: Materials Characterization, 2019. **10**(M19-7182).
55. Moore, E.A. and J. Readman, *Solid state chemistry: an introduction*. 2025: CRC press.
56. Epp, J., *X-ray diffraction (XRD) techniques for materials characterization*, in *Materials characterization using nondestructive evaluation (NDE) methods*. 2016, Elsevier. p. 81-124.
57. Núñez, A.M., et al., *Influence of PbCl2 and KCl salt mixture on high temperature corrosion of alloy 625.* Fuel, 2024. **358**: p. 130196.
58. Norling, R. and A. Nylund, *The Influence of Temperature on Oxide-Scale Formation during Erosion--Corrosion.* Oxidation of metals, 2005. **63**: p. 87-111.
59. Bale, C.W., et al., *FactSage thermochemical software and databases.* Calphad, 2002. **26**(2): p. 189-228.
60. Ting, J. and R.Y. Lin, *Molten carbonate-induced hot corrosion of nickel.* Oxidation of metals, 1989. **32**: p. 225-240.